Modeling Neuropathic Corneal Pain: Pulled Nerve Approach With Elevated *Krt16* Gene Expression

Mohd. Afzal Khan,[1] Gehan Fatima,[1] Acquah Emmanuel,[1] Sang Seong Kim,[1] Hyuk Sang Kwon,[1] Kyung Chul Yoon,[2] Young Ro Kim,[3] and Euiheon Chung[1,4]

[1]Department of Biomedical Science and Engineering, Gwangju Institute of Science and Technology, Gwangju, South Korea
[2]Department of Ophthalmology, Chonnam National University Medical School and Hospital, South Korea
[3]Department of Radiology, Harvard Medical School, Boston, Massachusetts, United States
[4]AI Graduate School, Gwangju Institute of Science and Technology, South Korea

Correspondence: Young Ro Kim, Department of Radiology, Harvard Medical School, 149 13th St., Charlestown, MA 02129, USA; yrkim@mgh.harvard.edu.
Euiheon Chung, AI Graduate School, Gwangju Institute of Science and Technology, 123 Cheomdan-Gwagiro, Buk-Gu, Gwangju 61005, South Korea; ogong50@gist.ac.kr.

Received: September 23, 2024
Accepted: January 21, 2025
Published: February 12, 2025

Citation: Khan MA, Fatima G, Emmanuel A, et al. Modeling neuropathic corneal pain: Pulled nerve approach with elevated *Krt16* gene expression. *Invest Ophthalmol Vis Sci.* 2025;66(2):35. https://doi.org/10.1167/iovs.66.2.35

Purpose. Neuropathic corneal pain (NCP) is a debilitating condition affecting millions of people worldwide. Despite their critical importance, currently available animal models for NCP research are limited by complex surgeries with high-risk strategy. To advance fundamental understanding of NCP, we developed a novel rodent model that explores both structural and functional mechanisms of the disease, offering a comprehensive approach.

Methods. By uplifting (2–3 mm transversely) the long ciliary nerve (LCN) with gentle force (0.09 ± 0.02 newton [N]) and pressure (0.18 ± 0.05 MPa), our pulled nerve model mimics human NCP conditions and was investigated alongside normal control, sham control, and full transection groups. Specifically, we quantified the NCP status by establishing a relationship between pain perception and chemical sensitivity, using Stevens' Power Law concept.

Results. Following surgery, the temporal patterns of heightened pain perception showed consistent trends across different stimulus methods, suggesting that von Frey and chemical tests could effectively evaluate pain progression. The discernable differences in Alpha values (exponent) of the pain-perception curves across the normal control, pulled nerve, and full transection groups (0.175 ± 0.035, 0.235 ± 0.015, and 0.275 ± 0.005, respectively) demonstrate the model's sensitivity to changes in NCP status. Histological analysis revealed LCN elongation, thickening, and corneal alterations in pulled nerve models, with reduced satellite glial cells (SGCs) in trigeminal ganglion compared to the normal control models. *Krt16* gene expression was significantly upregulated following pulled nerve surgery.

Conclusions. Our model not only delineates the pathological landscape of NCP but also promises to accelerate the development of targeted therapies.

Keywords: neuropathic corneal pain (NCP), animal pain model, pulled nerve, steven's power law, satellite glial cells (SGCs), pain-perception curve, *Krt16* gene

Neuropathic pain (NP) is defined as a pain that originates or is induced by a disease or debilitation of the nervous system.[1,2] A staggering 7% of the world's population suffers from a certain type of highly intractable NP,[1] in which the most prominent, common symptoms are sensory abnormalities, known as allodynia and hyperalgesia.[3] As an example of widespread NP type, NP in the cornea (neuropathic corneal pain [NCP]) disrupts the somatosensory system with one of the worst pain conditions with abnormally high local sensitivity causing extreme distress to the quality of human life.[4–8] NCP is a complex condition characterized by an abnormal pain response to typically non-painful stimuli.[9] NCP is a relatively novel and poorly understood condition within ophthalmology.[10] It has recently gained notable attention among clinicians and researchers due to a growing recognition of the condition, alongside a rising number of patients presenting with unexplained ocular surface pain and related symptoms.[4,11]

Of all human organs, the cornea is the most densely populated with sensory neurons with its neural activity extending throughout the entire cortex. With the presence of the referred pains, even the involvement of multiple organs (e.g. skin and visceral structures) and associated neural correlates is suggested upon dysfunctionalization of the sensory units in the development of NCP.[12] Clinically, several pathological conditions affecting ocular functions, such as acute infection, herpetic eye disease, dry eye syndrome, surgery, diabetes, stroke, and intracranial lesion, can systemically damage the corneal nerve and deteriorate its neural interactions.[13–17] A persistent epithelium defect caused by the dysfunctional corneal nerve may also promote dissolution of the cornea and eventually result in

tissue perforation, potentially leading to permanent blindness.[18,19]

For investigating pathophysiological mechanisms and searching for therapeutic interventions, a number of NCP models have previously been proposed and developed using various animal species.[20] However, these existing models have not been adequate due to the lack of complete, realistic NCP conditions. For instance, chemical models are likely to harm the corneal surface as they depend heavily on the topical application of the chemicals (e.g. alcohol or alkali), which cause acute epithelial damage in the cornea.[21] Because such extrinsic damage destroys all nerve endings, representation of the NCP progression is highly unrealistic (along with ocular burns and induction of dry eye disease [DED]). Additionally, another method, UV irradiation at the ocular surface, would incur damage not only to the corneal nerves but also to the unintended corneal keratocytes, as well as both epithelial and endothelial cells.[22] Nonetheless, ciliary axotomy and ligation models (e.g. temporal and transconjunctival approaches) have been useful for studying NCP as they exhibit altered behavior and sensory responses without epithelial damage.[23–25] However, these models also suffer from several drawbacks, such as surgical difficulties as ligation requires careful placement of a suture around the nerve, ensuring the correct tension so that the nerve is damaged but not severed, long recovery time which leads to postoperative complications, and incomplete NCP features because ligation might not fully prevent nerve conduction if it is too loose, leading to inconsistent results and exposure to the crucial vortex vein.[25]

The primary goal of our current study is to develop a practical mouse NCP model that overcomes the shortcomings of existing animal models. Methodologically, by transversely lifting the ciliary nerve with controlled force, we created a modified version of the ciliary nerve axotomy model and successfully demonstrated pathophysiological conditions of NCP. For verifying the development of NCP symptoms, behavioral tests were strategically performed to examine corneal sensitivity using both mechanical and chemical stimuli, in which Stevens' power law (concept not equation) was used to describe NCP-induced sensory modulation.[26]

To gain a deeper understanding of the molecular mechanisms underlying NCP, we used RNA sequencing (RNA-seq) to comprehensively profile gene expression changes. This approach revealed multiple genes potentially involved in the pathophysiology of NCP, including the elevated expression of Keratin 16 (*KRT16*), a marker commonly associated with epithelial stress responses. Although *KRT16* itself was not the primary focus of this study, its observed expression change underscores the complex alterations occurring within the corneal environment during NCP. Moreover, in the realm of epithelial cell biology, keratins play a pivotal role in maintaining cellular integrity and function. Among the various keratins, *KRT16* has garnered significant attention due to its essential role in the skin's protective barrier.[27] The *Krt16* genes are related to the mechanical strength of the epidermis,[28] conditions affecting hyperproliferative regions of the epidermis,[28,29] the process of corneal wound healing,[28,30] and a biomarker for complex regional pain syndrome (CRPS),[31] and pachyonychia congenital[32] treatment. In a pulled nerve model, the heightened expression of *KRT16* can provide insights into how the corneal epithelial cells adapt to and recover from mechanical injuries. The use of a newly designed rodent model and associated testing and analysis methods would robustly contribute to unveil mechanisms leading to the development as well as chronification of NCP while supporting the investigation of potential therapeutic interventions with quantitative pain assessment and high reproducibility. In this study, we first evaluated the behavioral responses associated with NCP using established sensitivity tests to characterize pain manifestations. Second, we explored corneal nerve morphology through detailed imaging and histological assessments to investigate structural changes linked to NCP. Finally, we examined molecular alterations by performing RNA-seq to identify differentially expressed genes and pathways that may contribute to NCP pathophysiology, thereby providing insights into potential therapeutic targets.

Materials and Methods

Animals

The handling of animals was conducted in accordance with the guidelines of Institutional Animal Care and Use Committee board (IACUC) of the Gwangju Institute of Science and Technology (GIST), South Korea. The Laboratory Animal Resource Center (LARC) at GIST approved the animal experimental protocol (Protocol Number: GIST-2021-036). *Thy1*-YFP transgenic mice (Stock No: 003709; Jackson Laboratory, Bar Harbor, ME, USA), with body weights of 20 to 25 g, were used. These mice were housed in the LARC and maintained under a 12-hour light/dark cycle with ad libitum access to food and water.

Animal Surgery

Animals were anesthetized with an intraperitoneal injection of zoletile/rompun (Zoletil/Xylazine) mixture in saline solution (60/10 mg/kg body weight). After confirming anesthesia with the tail pinch method, Neodex ophthalmic ointment (Hanlim Pharmaceuticals, South Korea) was applied to the eyes to prevent drying. The animals then underwent periorbital shaving and disinfection with povidone iodine, after which a 1.5 mm lateral canthotomy was performed.[18] Using Vannas scissors and conjunctival forceps, the lateral conjunctival fornix was incised at 90 degrees, care was taken to avoid injury to the retro-orbital venous plexus. Afterward, nasal eye rotation was performed, and preparation of muscles, and soft and connective tissues was prepared using conjunctival forceps. The long ciliary nerve (LCN), which branches from the trigeminal nerve, was identified approximately 0.3 to 0.4 mm from the exposed optic nerve.[15] Three animal groups were established: the first underwent full transection (the transection might be favored for its less technical complexity and skills as compared to the ligation method) of the LCN, the second experienced LCN pulling (pulled nerve), and the third underwent sham control surgery. The surgeries were performed unilaterally on the right eye of each animal. In the full transection group, a clearcut sideport knife (dual bevel, 1 mm angled, Alcon #8065921540) was used to transect the ciliary nerve, rotating the eye globe with forceps using the optic nerve as a landmark. For the pulled nerve model, the ciliary nerve was gently uplifted approximately 2 to 3 mm transversely from its position using an iris spatula (barraquer, 0.5 mm, Katena, K 3-2300) for 10 seconds, with a gentle force (~0.09 ± 0.02 newton [N]), which was

Investigative Ophthalmology & Visual Science

measured by the newton meter (Cat. No. A05-4065, Narika, Japan), as shown in Supplementary Figure S1 and pressure (~0.18 ± 0.05 MPa), considering the area as the area of iris spatula and the area of LCN. All procedures, except for the nerve injury steps, were repeated for the sham control surgery group. The incisions were closed with 6–0 Vicryl sutures. A drop of iodine solution was applied to the incision to prevent bacterial infection, and postoperatively the animals were placed on a heating pad.

Corneal Mechanical Sensitivity

Mechanical corneal sensitivity was assessed by applying varying forces to the center of the cornea in immobilized mice, using calibrated von Frey filaments (0.008–0.16 g).[33–35] The mechanical stimulation threshold, which induced an eye-blink response, was recorded when the von Frey filament was applied with pressure for 5 seconds. The ascending stimulus method involves starting with the filament that exerts the lowest force and applying it a set number of times (5 applications in this case). If the withdrawal response occurs less than 40% of the time (meaning none or only one withdrawal out of 5 applications), the next filament with higher force is tested. If the withdrawal response occurs 40% or more (i.e. 2 or more withdrawals out of 5 applications), the test is stopped, and the force of the last filament is recorded as the mechanical withdrawal threshold.[35] The tests were conducted at multiple time points: 1 day before surgery (D –1) and on days 1, 3, 5, 7, and 14 ($n = 5$ for each group). All experimental procedures were performed by the same experimenter, who conducted behavioral experiments under single-blind condition (the experimenter was unaware of the group allocations).

Corneal Chemical Sensitivity

To evaluate corneal chemical sensitivity, the eye-wiping test was used both before and after the surgery to determine the stimulation threshold. Ten microliters of hypertonic solution (NaCl 2M) were applied to the right eye of the mouse. Subsequently, the animal was placed in an individual cage.[34,36] The number of eye wipes performed with the forelimbs was counted over a 30-second period. Normal facial grooming episodes and wipes of the contralateral eye were not included in the eye wipe count. The tests were conducted at multiple time points: 1 day before surgery (D –1) and on days 1, 3, 5, 7, and 14 ($n = 5$ for each group). All experimental procedures were consistently performed by the same experimenter, who conducted the behavioral experiments under single-blind conditions.

Immunofluorescence Staining and Imaging (Ciliary Nerves)

Ciliary nerves were harvested on D –1 post-pulled nerve surgery ($n = 5$), and the mice were then euthanized. For visualization and analysis, the ciliary nerves were fixed in 4% paraformaldehyde (PFA) for 2 hours at 4°C. Following fixation, the samples were washed several times with PBS. For whole-mount immunofluorescence (IF) staining, the samples were blocked with 5% goat or donkey serum in 0.3% Triton X-100 in PBS (PBST) for 2 hours at room temperature (RT). The samples were then incubated overnight at 4°C with the indicated primary antibodies diluted in the blocking solution. After several washes with PBST, the samples were incubated for 2 hours at RT with the indicated fluorochrome-conjugated secondary antibodies, also diluted in the blocking buffer. After additional washes with PBST, the samples were mounted using Vecta-shield (Vector Laboratories) fluorescence mounting medium. The primary and secondary antibodies used were as follows: anti-neurofilament 200 (1:200, rabbit polyclonal, N4142, Sigma-Aldrich) and Alexa 488-conjugated secondary antibodies (1:500, Invitrogen). Images were obtained using an LSM 800 confocal microscope (Carl Zeiss) and processed with ZEN (Zeiss) imaging software. Three-dimensional reconstructions of the labeled ciliary nerve were prepared using Imaris software (Supplementary Fig. S4A, version 9.7.0; Bitplane AG, Zurich, Switzerland).

Immunofluorescence Staining and Imaging (Corneal Nerves)

Corneas were harvested on D3 and D7 post-surgery ($n = 3$, each group). For visualization and analysis, the corneas were fixed in 4% PFA for 2 hours at 4°C. Following fixation, the samples were washed several times with PBS. For whole-mount IF staining, the samples were blocked with 5% goat or donkey serum in 0.3% Triton X-100 in PBS (PBST) for 2 hours at RT. The samples were then incubated overnight at 4°C with the indicated primary antibodies diluted in the blocking solution. After several washes with PBST, the samples were incubated for 2 hours at RT with the indicated fluorochrome conjugated secondary antibodies, also diluted in the blocking buffer. After additional washes with PBST, the samples were mounted using Vecta-shield (Vector Laboratories) fluorescence mounting medium. The primary and secondary antibodies used were as follows: anti-beta tubulin (1:200, rabbit polyclonal, ab18207, Abcam) and Alexa 488-conjugated secondary antibodies (1:1000, Invitrogen), respectively. Images were obtained using an LSM 800 confocal microscopes (Carl Zeiss) and processed with ZEN (Zeiss) imaging software.

Immunofluorescence Staining and Imaging (*Krt 16* Gene)

Corneas were excised and fixed with 10% formaldehyde in 1 × phosphate-buffered saline, and then the corneal sections (15 µm thick) were prepared using Cryostat. The sections next were permeabilized with 0.3% Triton X-100 for 15 minutes and blocked with 5% goat or donkey serum in 0.3% Triton X-100 in PBS (PBST) for 2 hours at RT. The samples were then incubated overnight at 4°C with the indicated primary antibodies diluted in the blocking solution. After several washes with PBST, the samples were incubated for 2 hours at RT with the indicated fluorochrome conjugated secondary antibodies, also diluted in the blocking buffer with nuclear dye Hoechst. After additional washes with PBST, the samples were mounted using Vecta-shield (Vector Laboratories) fluorescence mounting medium. The primary and secondary antibodies used were as follows: Cytokeratin 16 (1:200, rabbit polyclonal, 17265-1-AP Proteintech) and Alexa 488-conjugated secondary antibodies (1:1000, Invitrogen), respectively. Images were obtained using an LSM 800 confocal microscopes (Carl Zeiss) and processed with ZEN (Zeiss) imaging software.

Investigative Ophthalmology & Visual Science

Histology Staining

Two weeks after the experiments (on day 15), the mice were euthanized ($n = 5$ for each group), and, subsequently, their trigeminal ganglion and eyes were collected and fixed in 4% PFA. For hematoxylin and eosin (H&E) staining, the sample slices were refixed, washed, and stained with H&E.

Corneal Fluorescein Staining

Fluorescein solution was prepared by reconstituting 0.4 M of fluorescein strip in 0.8 mL of 1X PBS and again mixed it with 100 mL of 1X PBS resulting in a 0.1% fluorescein solution ($n = 5$ for each group) and the analysis was performed using National Eye Institute (NEI) scoring[37] on day 3, day 5, and day 7.

RNA Isolation and Sequencing

Corneal tissue RNA was isolated on day 15 (D15) using the standard TRIzol LS (#10296028 Invitrogen) extraction protocol ($n = 6$ for each group). This was followed by treatment with RQ1 RNase-free DNase (Promega) and further purification using TRIzol LS (Ambion). RNA quality was assessed using an Agilent Bioanalyzer. Sequencing libraries were constructed for polyadenylated RNA using the Dynabeads RNA Purification Kit (Thermo Fisher Scientific) and the TruSeq Stranded Total RNA Gold Library Kit (Illumina), following the manufacturer's instructions. IDT for Illumina TruSeq UD indexes were incorporated, and high-throughput sequencing was performed on an Illumina NovaSeq 500, generating 150-nucleotide paired-end reads.

Real-Time Quantitative PCR Analysis

Total RNA was extracted from the cornea on D15 using the standard TRIzol (Invitrogen) extraction protocol ($n = 6$ for each group), followed by treatment with RQ1 RNase-free DNase (Promega) and further purification using TRIzol (Ambion). The extracted RNA was reverse transcribed into first-strand cDNA using the High-Capacity cDNA Reverse Transcription Kit (Thermo Fisher Scientific). A 1 µL template of the synthesized cDNA was amplified by real-time PCR using the primers listed in Supplementary Table S1 (Integrated DNA Technologies). Each sample was run in triplicate in a 20 µL reaction containing 250 nM forward and reverse primers, 10 µL of amfiSure qGreen Q-PCR Master Mix (2X; GenDepot, US) and 20 ng of cDNA. Reactions were carried out using a BIO-RAD CFX96 real-time PCR system. The target genes included *Saa3*, *Krt16*, and *Lcn2*, with Gapdh was used as an internal control for normalization due to its demonstrated stability following peripheral nerve injury (see Supplementary Table S1). Specific primers for *Krt16* were designed based on the mouse *Krt16* gene sequence, forward sequence: (AGAACCTCAATGACCGCCTG) and reverse sequence: (TCAGGTCCTCAATGGTCTTG). Ratios of ipsilateral-side mRNA levels to contralateral-side mRNA levels were calculated using the ΔCt method ($2-\Delta\Delta Ct$).

Functional Enrichment Analysis

Gene Ontology Biological Processes (GO-BP), Gene Ontology Cellular Component (GO-CC), Molecular Function, and Kyoto Encyclopedia of Genes and Genomes (KEGG) Pathway enrichment analyses were performed using the DAVID[38] web database tool. These analyses were conducted to identify the processes and pathways regulated by the differentially expressed genes (DEGs). Enriched terms were identified using a cutoff criterion of adjusted P value ≤ 0.05.

Network Construction and Hub Identification

The protein–protein interaction (PPI) networks were constructed for the significant DEGs using the Search Tool for the Retrieval of Interacting Genes/Proteins (STRING) database version 12.0 with default parameters. The interactions from the STRING database were exported to Cytoscape[39] version 3.10.2 and the top 20 protein hubs were identified using the Maximal Clique Centrality (MCC) algorithm of the CytoHubba plugin. The PPI of four MCODE complexes identified in Metascape.[40]

Statistical Analysis

The results were expressed in mean ± SD. Data analysis was performed using GraphPad Prism9 (GraphPad, San Diego, CA, USA). Differences in mechanical and chemical corneal sensitivities before and after surgery for the ipsilateral eye were evaluated using a paired t-test. Each group consisted of five animals ($n = 5$). For the analysis of H&E staining images, Image J (Fiji) and Aperio image Scope (version 12.4.6.5003) software were utilized to calculate the total number of neuronal bodies, satellite glial cells, Schwann cells, and the thickness of corneal layers. We performed our analysis from ophthalmic, V1 region only (Supplementary Fig. S2).[41] Five animals from each group were used for staining ($n = 5$). Statistically significant differences were indicated as follows: $^{*}P < 0.05$, $^{**}P < 0.01$, $^{***}P < 0.001$, $^{****}P < 0.0001$; "n.s." denotes no significant difference.

Results

Anatomy of LCN and Descriptions of NCP Model Production

Understanding the anatomy of LCN is crucial for studying ocular sensory pathways, vision-related disorders, and potential therapeutic interventions targeting ocular sensory innervation. Its role in relaying sensory information underscores its significance in maintaining ocular health and function. The LCN in the mouse is a slender branch of the ophthalmic nerve, a division of the trigeminal nerve (Fig. 1A). Anatomically, LCN traverses through the posterior aspect of the globe, piercing the sclera close to the optic nerve. It carries sensory fibers responsible for conveying sensations from the cornea. Performing the surgical procedure to pull the LCN in mice requires precision and care to avoid damage to surrounding structures (Supplementary Fig. S3). Listed in Figure 1A are the force and duration parameters used for pulling the LCN. Throughout the process, maintaining the aseptic condition, using proper magnifications, and delicate handling of tissue are critical for the successful surgery of the pulled nerve model (Fig. 1B). To evaluate the progression of NCP, behavioral tests were conducted on a single mouse over a period from D –1 to D14 post-surgery. The von Frey test and the eye-wiping test were utilized to measure mechanical and chemical corneal sensitivity, respectively (Fig. 1C). The corneal sensitivity to the NaCl solution was examined by counting the number of eye

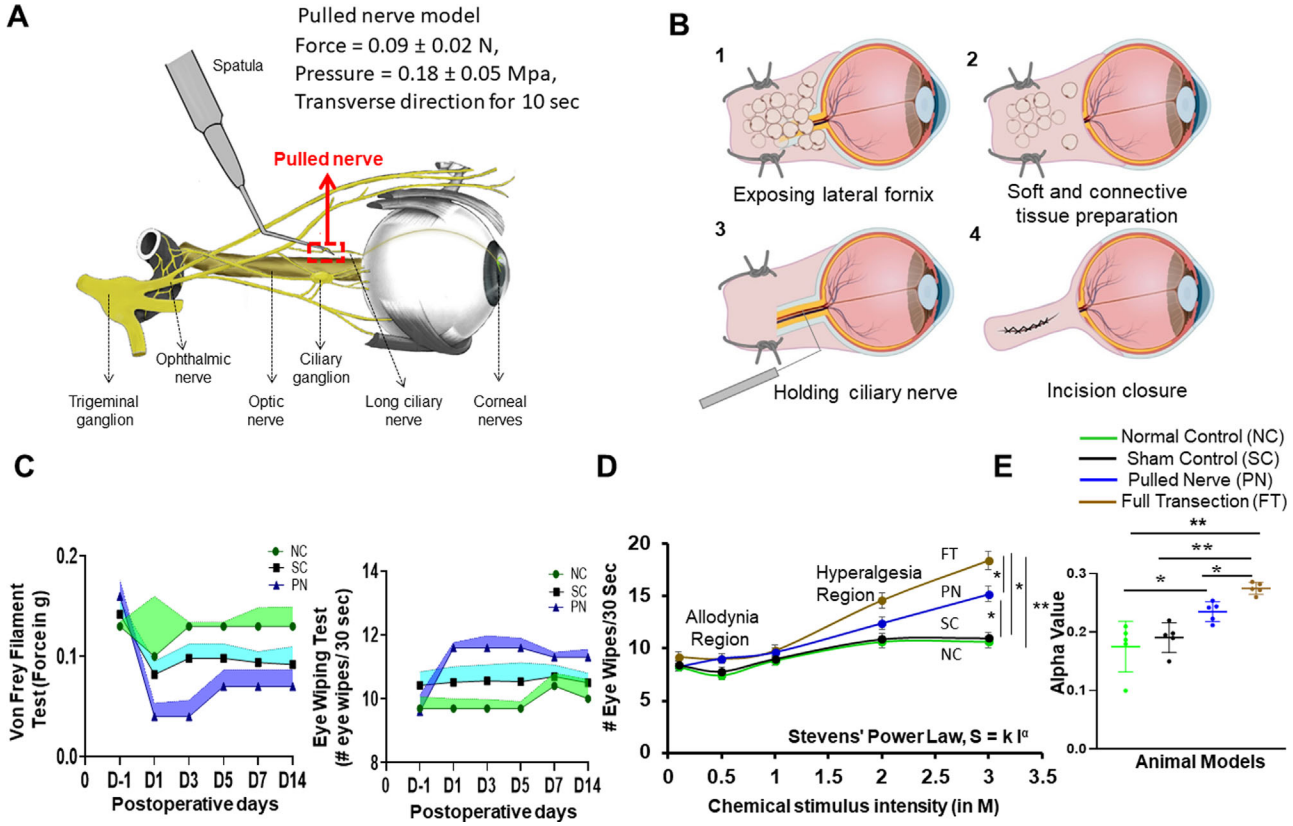

Figure 1. Illustrations depicting the anatomical exploration of long ciliary nerve (LCN) and its surrounding structures in the pulled nerve (PN) model, alongside the development of post-surgical neuropathic corneal pain (NCP). (**A**) Schematics depicting nerve networks, with emphasis on the trigeminal nerve branches with the ophthalmic branch, leading to the LCN, which plays a significant role in corneal sensation. Manipulation of the LCN was performed with the designed parameters in the pulled nerve (PN) model. (**B**) Surgical procedures for the PN model. (1) Lateral fornix exposure: eye globe dislocation facilitated by a lateral canthotomy. (2) Preparation of soft and connective tissue: an incision at the lateral fornix with preservation of the limbal conjunctiva. (3) Ciliary nerve manipulation: application of a gentle force to the ciliary nerve for 10 seconds. (4) Closure of the surgical area with vicryl suture. (**C**) Behavioral testing to assess trends in NCP underscoring the importance of longitudinal behavioral assessments in understanding the progression of neuropathic pain in the cornea. (**D**) Quantitative assessment of neuropathic pain ($n = 5$ for each model group), showing the relationship between perceived pain levels and chemical stimulus intensity at postoperative day 1 (D1) for normal control (NC), sham control (SC), pulled nerve, and full transection (FT) models. (**E**) Psychological magnitude functions determined by the alpha value for each model using regression analysis ($n = 5$ for each model group), indicating that pain sensation correlates to chemical stimulus intensity in accordance with Seven's power law (S = sensation magnitude, k = constant, I = stimulus intensity, and α = Power exponent dependent on modality). Statistical significance is denoted as $^{*}P < 0.05$, $^{**}P < 0.01$, $^{***}P < 0.001$, $^{****}P < 0.0001$, n.s. = not significant.

wipes for 30 seconds, accompanied by the forelimb movement of the animal. For each challenge, a 10 µL drop of NaCl solution of varying concentrations (i.e. 0.1, 0.5, 1, 2, and 3 M) was applied to the ipsilateral eye in the normal control, the pulled nerve, and the full transection models (Fig. 1D). As shown in Figures 1D and 1E, the power exponents in psychological magnitude functions (using alpha exponential function) were 0.175 ± 0.035, 0.235 ± 0.015, and 0.275 ± 0.005 at D1 for the normal control, pulled nerve, and full transection models, respectively.

NCP Decreased Mechanical and Increased Chemical Sensitivities Assessed by Behavioral Responses to External Stimuli

Behavioral alterations based on responses to external stimuli were used to assess the perception level of NCP. Illustration outlining the setup and timeline of von Frey filament test and eye wipe test (EWT), for measuring corneal mechanical sensitivity thresholds (g) and chemical pain response, respectively, before and after surgery are shown in Figures 2A and 2B, including the surgery of 8 week old mice, and the collection of histology samples after 2 weeks from the surgery. The pre-surgery corneal mechanical sensitivity threshold (g) was measured in the ipsilateral eye (before and after surgery) at D –1 (baseline), where no significant differences in the threshold were observed across all four groups. In the pulled nerve model, the D1 reading (0.046 ± 0.013 g) showed that the threshold force applied by the von Frey filament decreased by 67.7%, compared to the D –1 value (0.142 ± 0.016 g), whereas for the full transection model, it was 80.1% (D1 reading, 0.028 ± 0.010 g and D–1 value 0.142 ± 0.016 g). The full transection and pulled nerve groups exhibited 65.7 and 43.1% decreases (0.028 ± 0.012 and 0.046 ± 0.013 g), respectively, compared to the sham control group (0.082 ± 0.013 g) on D1 (Fig. 2C). In both the full transection and pulled nerve models, the von Frey threshold remained suppressed throughout the post-surgery experiment dates (up to 2 weeks). A noticeable, statistically

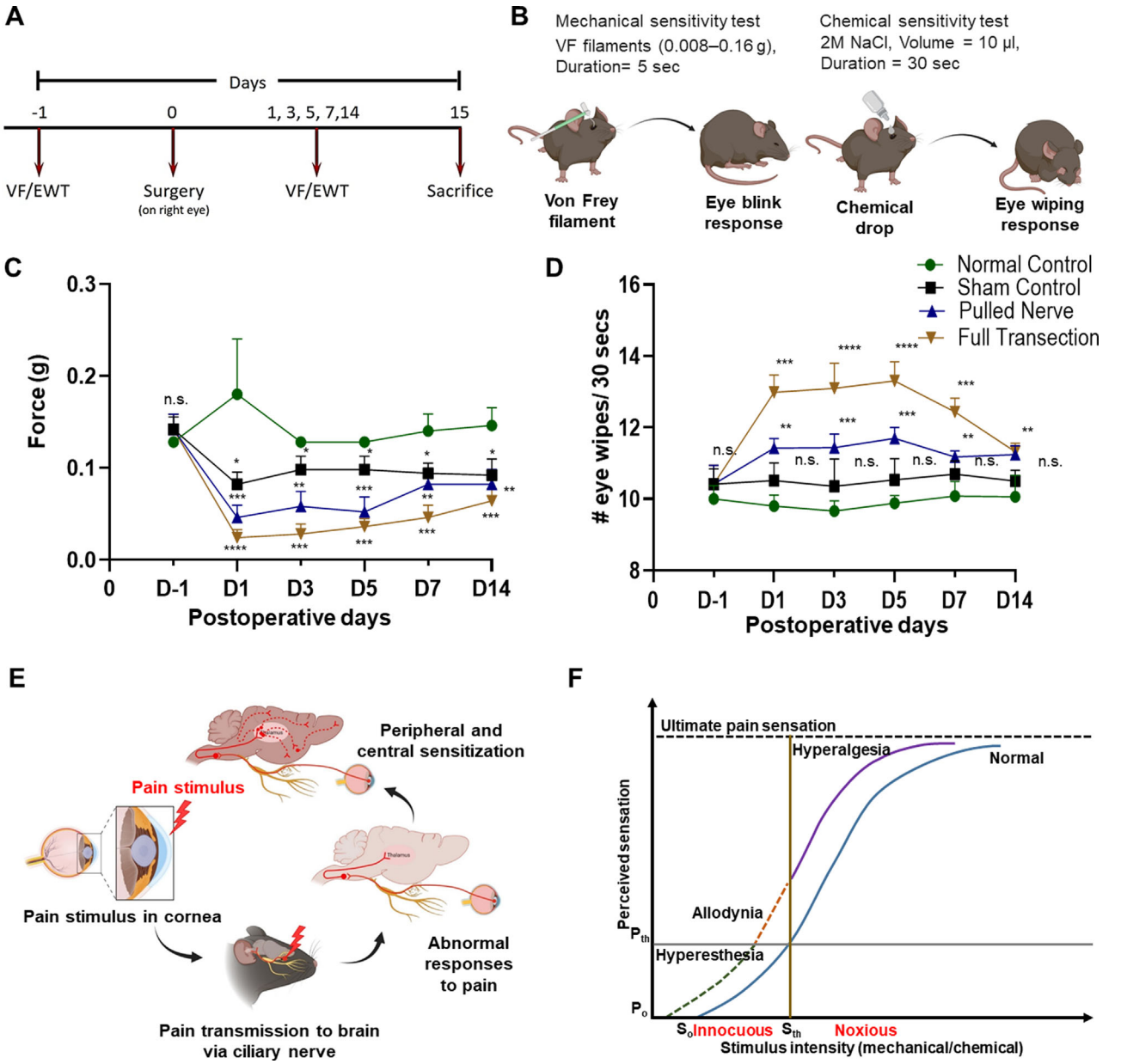

Figure 2. Assessment of behavioral responses in mice using von Frey (VF) filament and eye wiping test (EWT). (**A**) Diagram illustrates the experimental timeline including VF filament test and EWT, surgery, and terminal procedures using 8 weeks old mice. (**B**) Illustration of VF and EWT test for assessing pain. Calibrated filaments exert forces (0.008–0.16 g) on the central cornea of restrained mice, with the mechanical threshold determined by the eye-blink response, whereas for the chemical behavior test procedure mice are acclimated in a new cage for 5 minutes before applying one drop (10 µL) of 2 M NaCl solution to the cornea. The resulting eye wipes are counted over a 30-second period. (**C**) Mechanical sensitivity ($n = 5$ for each model group): corneal sensitivity was evaluated for the ipsilateral eye in normal control, sham control (SC), pulled nerve, and full transection models. The corneal mechanical sensitivity threshold (g) is represented by mean values (±SD) from day –1 to day 14 post-surgery. (**D**) Chemical sensitivity ($n = 5$ for each model group): for normal control, sham control, pulled nerve, and full transection models. The corneal chemical sensitivity threshold (g) is represented by mean values (±SD) from day −1 to day 14 post-surgery. Statistical significance is denoted as $^{*}P < 0.05$, $^{**}P < 0.01$, $^{***}P < 0.001$, $^{****}P < 0.0001$, n.s. = not significant. (**E**) Schematic illustrating the transmission of an external stimulus from the cornea to the brain via the long ciliary nerve. Abnormal pain responses (hyperalgesia or allodynia) are activated prior to conversion into peripheral and central sensitization. (**F**) The representative graph showing specific symptoms of neuropathic pain in relation to pain sensation and external stimulation. Values for pain and stimulus value at zero (P_o and S_o, respectively) and at threshold (P_{th} and S_{th}, respectively) are depicted. The two prominent symptoms of neuropathic pain, allodynia and hyperalgesia, are compared to the normal response.

significant longitudinal increase of von Frey thresholds was observed between D5 and D7 (0.052 ± 0.016 and 0.082 ± 0.012 g, respectively) for the pulled nerve group. In addition, similar increases were observed in the full transection group for the entire post-surgery dates with statistical significances. At D14, the von Frey thresholds of all 3 surgery groups appear to converge, particularly with statistically significant improvements over the D1 to D14 period

for the pulled nerve and the full transection groups, possibly to a common chronic sensitization stage. There were no significant differences found on the contralateral side in each model (see Supplementary Fig. S4).

Before surgery at D–1, no significant differences were observed among the 3 groups in the chemical behavior test. Unlike the von Frey, the sham control results were not differentiable from the normal control group results throughout the study period. The pulled nerve group data (10.42 ± 0.52 and 11.48 ± 0.16 at D –1 and D1, respectively) showed a 10.1% increase in the number of eye wipes, whereas the sham control group (10.42 ± 0.42 and 10.52 ± 0.48 at D –1 and D1, respectively) was insignificant (Fig. 2D). Compared to the D –1 (10.42 ± 0.52) values, the D1 data of the full transection model (13.04 ± 0.51) showed a 30.1% increase in the number of eye wipes. In both the full transection and the pulled nerve models, the corneal chemical sensitivity remained significantly increased throughout the measurements. Meanwhile, the full transection group displayed certain statistically significant decreases among D5, D7, and D14. In general, increasing NaCl concentration increased the number of wipes. There were no significant differences found on contralateral side in each model (Supplementary Fig. S5). The hypothetical diagram illustrates how all these external stimulus affects the cornea with the signaling pathway through the LCN (Fig. 2E). This neural processing is likely disrupted, resulting in abnormal pain reactions such as heightened sensitivity (hyperalgesia) and/or pain from typically non-painful stimuli (allodynia), which progress into the sensitization of relevant nerves in both peripheral and central nervous systems (see Figs. 2E, 2F). In the pulled nerve model, the LCN does not fully restore to its normal condition within the 56-day observation period (Supplementary Fig. S6).

Morphological Changes of LCN After PN Surgery

To access and study the anatomy of LCN, the LCN was carefully isolated from the surrounding tissues. The LCN (dashed lines) in the pulled nerve model is displayed in Figure 3A. The temporal and nasal sides are marked to display proper anatomy and landmarks for locating the LCN. The width and length of the LCN were recorded at D1 as we grossly examined the structural integrity of the LCN under a stereomicroscope (Fig. 3B). NF200, a neurofilament marker, showing the nerve fibers one day after surgical intervention (Fig. 3C). NF200 staining reveals the distribution and integrity of the nerve fibers between the ipsilateral and contralateral sides, as shown in three-dimensional reconstruction of the NF200-stained ciliary nerve (Supplementary Fig. S7). The temporal (Fig. 3D) and nasal side widths (Fig. 3E), and total length (Fig. 3F) were significantly different between ipsilateral and contralateral LCNs. At D1, the ipsilateral temporal and nasal widths, and length of LCN were 86.14 ± 4.9 µm, 130.72 ± 19.25 µm, and 5.09 ± 0.58 mm, exhibiting 1.52-, 1.54-, and 1.21-fold increases when compared to the contralateral values (57.72 ± 12.14 µm, 84.7 ± 28.93 µm, and 4.19 ± 0.59 mm, respectively).

Histopathology Revealed Deformation of Corneal Layers in NCP Models

The H&E staining were performed to investigate the altered tissue structures and damage in the corneas collected at D15. As a result, the corneal tissue structures were altered in all three animal groups, in which abnormal cell morphologies were observed (Fig. 4A). Across all three groups, corneal epithelia were characterized by structural alterations, displaying different degrees of damage patterns, specific for each model. The stroma was well connected with the endothelial layer for all three groups. However, the shrunken remnants of epithelium composed of damaged cells were apparent in the full transection models, whereas detachment of the epithelial layers from the stromal layers was evident for the pulled nerve models (Supplementary Table S2). In the sham control group, both the endothelium and epithelium were connected with the stroma, exhibiting no apparent changes as compared to the normal control group. When compared to the normal control group (18.22 ± 0.33 µm), statistically significant 66, 20.04, and 1% decreases (i.e. 6.1 ± 1.88, 14.34 ± 1.1, and 16.58 ± 0.79 µm) were observed in the corneal epithelial thickness for the full transection, pulled nerve, and sham control models, respectively (Fig. 4B). When compared to the normal control group (71.82 ± 0.84 µm), the corneal stromal thickness increased by statistically significant 53% and 40% increases and a negligible amount for the full transection, pulled nerve, and sham control models (i.e. 104.6 ± 2.08, 99.04 ± 3.74, and 70.9 ± 1.26 µm, respectively; Fig. 4C). When compared to the normal control group (1.9 ± 0.33 µm), there were 1.2% decreases for the full transection models, and 2.4% increases for the pulled nerve models, and 3.3% for the sham control models (i.e. 1.79 ± 0.512, 1.68 ± 0.676, and 1.58 ± 0.344 µm for the full transection, the pulled nerve group, and the sham control group, respectively) without any statistical significance in the corneal endothelial thickness (Fig. 4D). The relative percentage thickness of each model between the corneal layers was displayed (Fig. 4E). After pulled nerve surgery, there was no observable damage to the ocular surface based on the corneal fluorescein staining (Fig. 4F). There was no significant difference in staining between the normal control (baseline) and pulled nerve (days 3, 5, and 7) models (Fig. 4G) following NEI scoring criteria.

Histopathology of Trigeminal Ganglion Revealed Alteration of Neurons and Satellite Glial Cells

Schematic representation of H&E staining of the trigeminal ganglion (TG; Fig. 5A) illustrates the distinct structural organization of the TG. The longitudinal sections of the TG (Fig. 5B) focus specifically on the V1 region, ensuring anatomic accuracy and relevance to the study objectives. In all three experimental groups, modifications in TG tissue structures were observed, including irregularities in the number and distribution of neurons and satellite glial cells (SGCs). In the normal control model, the TG shows normal and healthy organization, in which neurons and SGCs are evenly distributed, without inflammation and cellular abnormalities. The SGCs were observed encircling neuronal cell bodies. Furthermore, Schwann cells were observed in association with neuronal fibers (Fig. 5C, higher magnification insets). TGs of the sham control model appear similar to those observed in the normal control group as no significant changes were observed in cellular morphology or organization, as well as in the number of neurons, SGCs, and Schwann cells (Figs. 5D, 5E, 5F). In the PN model, among the cell types, only the number of TG-SGCs exhibited a significant reduction (see Fig. 5E), whereas no significant

Investigative Ophthalmology & Visual Science

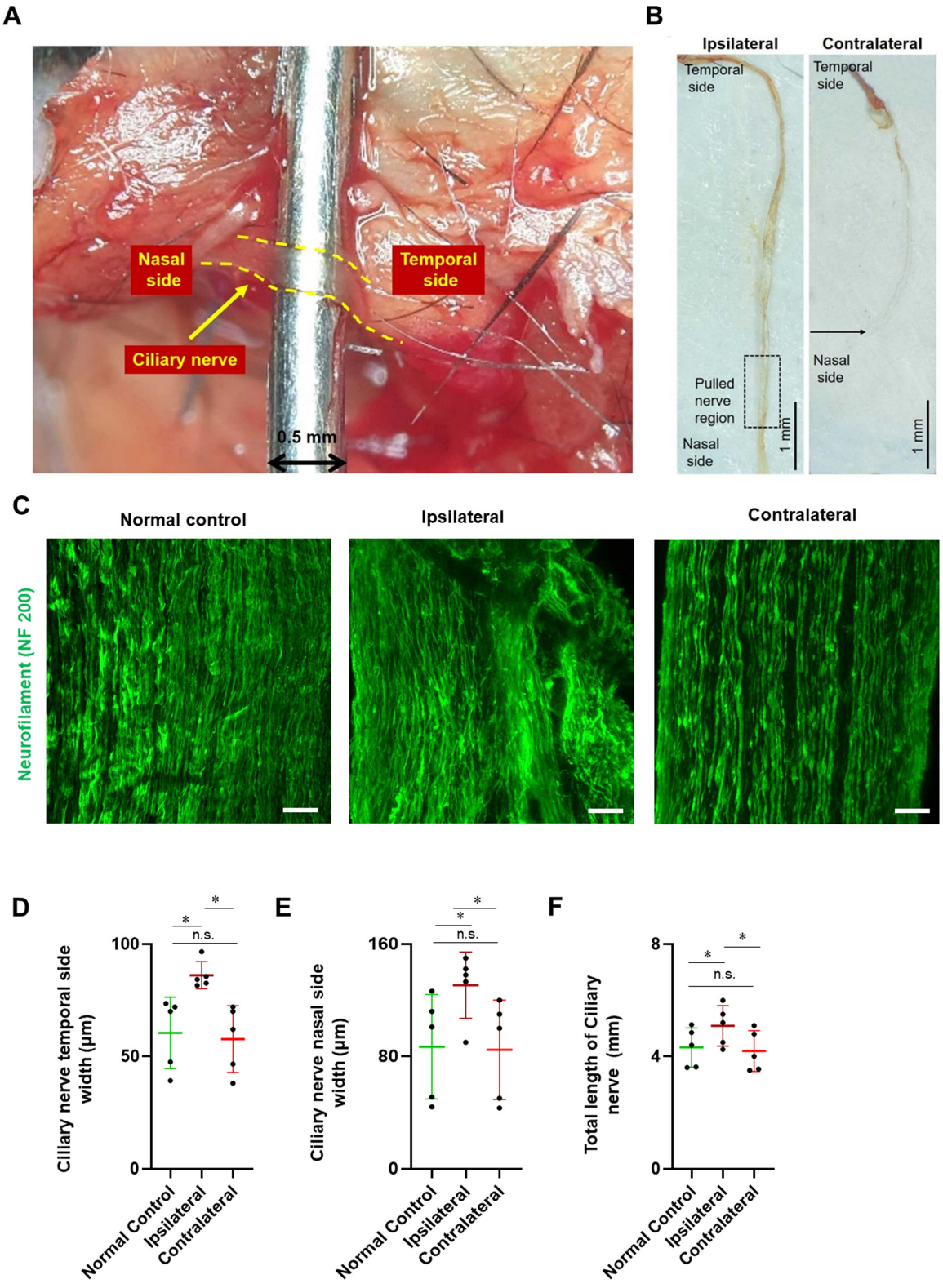

Figure 3. Dissection and analysis of NCP-affected long ciliary nerve (LCN). (**A**) The image shows the LCN (with *yellow dashed lines*) of a mouse. Temporal and nasal sides are indicated for anatomic orientation. The LCN was lifted approximately 2 to 3 mm from its original position for 10 seconds using an iris spatula, with gentle force (−0.09 ± 0.02 N) and pressure (−0.18 ± 0.05 MPa) for the pulled nerve model. (**B**) The dissected LCN from the pulled nerve model at postoperative day 1 (D1). The ipsilateral side shows an elongated and thickened ciliary nerve compared to the contralateral side, with the region pertaining to the lifted nerve section marked by a rectangle. (**C**) Immunofluorescence images of the ciliary nerve stained with NF200, a neurofilament marker, showing the nerve fibers 1 day after surgical intervention (pulled nerve). The images compare the ipsilateral and contralateral sides of pulled nerve with normal control, revealing the distribution and integrity of the nerve fibers ($n = 5$ in each model). NF200 staining highlights the structural differences between the two sides, with noticeable alterations in the ipsilateral side. Scale bar = 20 μm. (**D**, **E**, **F**) Measurements of temporal side width, nasal side width, and total length (μm) of the LCN in the normal control model and the pulled nerve model. Data points represent the mean values (±SD) for n = 5 mice at D1 post-surgery in the pulled nerve model. Statistical significance is indicated by $^{*}P < 0.05$, $^{**}P < 0.01$, $^{***}P < 0.001$, $^{****}P < 0.0001$.

Investigative Ophthalmology & Visual Science

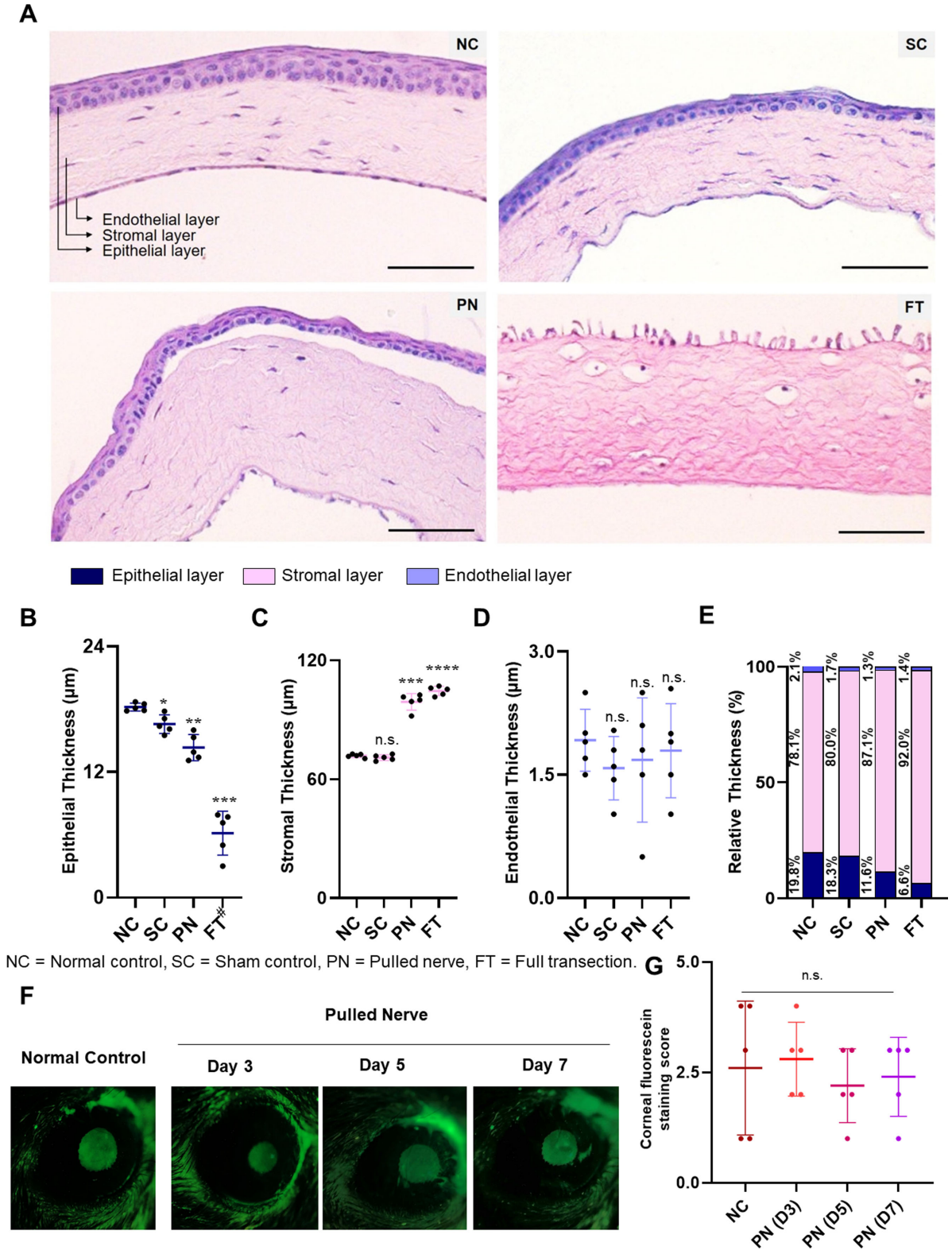

Figure 4. Corneal histopathology in NCP models using hematoxylin and eosin staining. (**A**) H&E stained cornea sections from normal control, sham control, pulled nerve, and full transection. Scale bar represents 50 µm. (**B**) Assessment of corneal integrity based on H&E staining: measurements of epithelial thickness (µm), (**C**) stromal thickness (µm), and (**D**) endothelial thickness (µm). (**E**) The relative thickness (%) of each corneal layer compared across different models. In the full transection model, the thickness of the epithelial layer was calculated by drawing an imaginary line at the base of epithelial remnants. Data points represent measurements from five mice in each model. Statistical significance is denoted as $^{*}P < 0.05$, $^{**}P < 0.01$, $^{***}P < 0.001$, $^{****}P < 0.0001$, n.s. = not significant. (**F**) Corneal fluorescein staining stereo axio zoom microscopy images depicting the cornea from both the normal control and the pulled nerve models. (**G**) Quantitative analysis of corneal fluorescein staining using the NEI scale (n = 5 mice in each model) on baseline (normal control) and day 3, day 5, and day 7 (pulled nerve). Statistical significance is denoted as $^{*}P < 0.05$, $^{**}P < 0.01$, $^{***}P < 0.001$, $^{****}P < 0.0001$, n.s. = not significant.

Investigative Ophthalmology & Visual Science

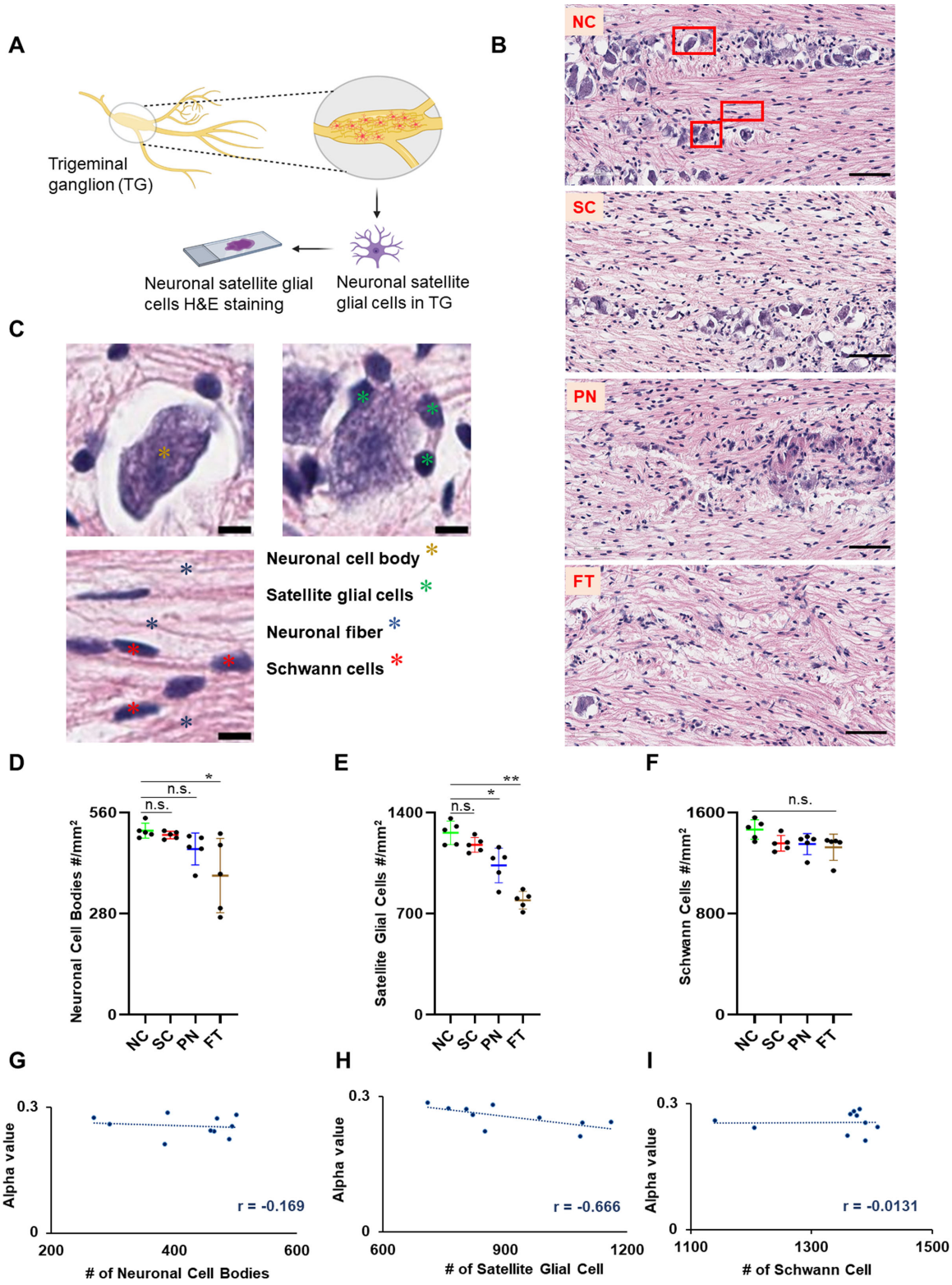

Figure 5. Histological analysis of the trigeminal ganglion using hematoxylin and eosin staining. (**A**) Schematic illustration of a trigeminal ganglion neuron, highlighting satellite glial cells and their depiction in H&E staining. (**B**) Longitudinal sections of the ganglia stained with H&E in normal control, sham control, pulled nerve, and full transection models from the V1 region are represented. (**C**) Satellite glial cells are shown surrounding neuronal cell bodies, with Schwann cells associated with neuronal fibers. Scale bars = main image 60 µm; insets = 6 µm. (**D**, **E**, **F**) Quantitative evaluation of neuronal cell body counts, satellite glial cell counts, and Schwann cell counts per mm^2 of ganglion area, respectively (# denotes number). (**G**, **H**, **I**) Psychological magnitude functions determined by the alpha value in relation to the neuronal cell body, satellite glial cell, and Schwann cell, respectively, for full transection and pulled nerve model displaying their *r* (Pearson correlation) value. Regression correlation value for the neuronal cell body, the satellite glial cell, and the Schwann cell, respectively, is −0.169, −0.666, and −0.0131. Data points represent mean values (± SD) for 5 mice (in each model) at D15 post-surgery. Statistical significance is denoted as $^{*}P < 0.05$, $^{**}P < 0.01$, $^{***}P < 0.001$, $^{****}P < 0.0001$, n.s. = not significant.

Investigative Ophthalmology & Visual Science

changes were observed in the numbers of neuronal cell bodies and Schwann cells (see Figs. 5D, 5F). For the full transection model, the numbers of both neurons and SGCs in TG decreased significantly compared to the normal control group (see Fig. 5D), with signs of severe damage showing conspicuously irregular cell bodies, whereas no change was observed for Schwann cells (see Fig. 5F). Upon correlating alpha values acquired from the EWT results with the numbers of cells, strong exponential correlations were found between alpha values and either the number of neuronal cell bodies or that of SGCs, whereas no such correlation was found for Schwann cells. Combined data revealed a negative correlation between alpha values and the neuronal cell bodies, SGCs, and Schwann cells with r values of −0.169, −0.666, and −0.0131, respectively.

Gene Expression Alterations in the Pulled Nerve Model of NCP

A comprehensive analysis of gene expression in the corneal tissue of the normal control models and the pulled nerve models underscoring the extensive molecular changes associated with NCP (Supplementary Figs. S8A, S8B, S9A). Corneal RNA was isolated from both the normal control and pulled nerve models, followed by next-generation sequencing (NGS) to identify gene expression profiles (Fig. 6A). The analysis revealed a substantial number (439) of genes significantly upregulated (230) and downregulated (209) in the pulled nerve model compared to the normal control model (Fig. 6B). This is visualized in a volcano plot (Fig. 6C), where the red and blue dots indicate significantly upregulated and downregulated genes, respectively. Hierarchical clustering (Fig. 6D) highlighted distinct gene expression patterns between the normal control and the pulled nerve models. The heat map shows normalized and variance-stabilized values of DEGs. The Gene Ontology (GO) analysis revealed several processes that were affected in the PN versus the normal control models, including immune system process, inflammatory response, neutrophil chemotaxis, and tissue repair processes. Additionally, major cellular components, such as extracellular region, extracellular space, cornified envelope, and high-density lipoprotein particles were also prominently affected (Figs. 6E, 6F, 6G). Notably, genes involved in inflammation, immune response, and extracellular matrix organization were prominently affected. A hypothetical schematic (Fig. 6H) integrates these findings, suggesting that NCP involves a complex interplay of inflammation, immune response, and tissue repair processes. Key genes, such as *Saa3*, *Lcn2*, and *Krt16*, were highlighted for their roles in these processes, indicating their potential as therapeutic targets. The key metrics for the *Krt16* gene are, fold change (FC) = 27.79, log2 FC = 4.79, and adjusted P value = 2.69E-09. This indicates that the expression level of *Krt16* in the pulled nerve model was approximately 28 times higher, nearly 5-fold higher on a log2 scale and the extremely low P value confirms that the upregulation of *Krt16* is statistically significant and not due to random variation, than that in the normal control model.

Key Pathway Identification and Gene Expression Validation by qRT-PCR

The RNA-seq findings validated through qRT-PCR focused on key genes implicated in NCP. The heat map (Fig. 7A) displays the top 20 most abundant transcripts identified between the normal control and pulled nerve models. Variations in expression levels are color-coded, with red indicating increased expression and blue indicating decreased expression in the pulled nerve model. KEGG analysis revealed significant enrichment of the differentially expressed genes in pulled nerve (see Supplementary Fig. S9B), with the top 3 pathways involving calcium signaling, IL-17 signaling pathways, and cytokine-cytokine receptor interaction. These pathways were confirmed by GSEA (KEGG pathways) plot, showing a positive correlation with the pulled nerve model (Fig. 7B). Metascape analysis identified four MCODE complexes (Fig. 7C), representing tightly connected gene clusters with functional relevance. Additionally, hub genes were determined using the cytoHubba plugin in Cytoscape (Fig. 7D), highlighting key genes within the network. The bar charts compare mean values from RNA-seq and qRT-PCR for *Saa3*, *Lcn2*, and *Krt16* (Figs 7E, 7F, 7G, respectively). Several of the significant changes in gene expression between the normal control and pulled nerve models includes *Saa3*, *Lcn2*, and *Krt16*, which were validated by qRT-PCR analysis. There was a substantial increase in *Krt16* expression in the pulled nerve group, at D15 with a 2.1-fold increase compared to the normal control group. In addition, these data show strong consistency between the RNA-seq and qRT-PCR, with significant differences in gene expression among normal control, pulled nerve contralateral, and pulled nerve ipsilateral samples.

Corneal Nerve Alterations and *Krt16* Expression in Corneal Epithelium in the Pulled Nerve Model of NCP

Confocal imaging of corneal nerves stained with anti-β-tubulin revealed significant differences in nerve morphology across the normal control group and the pulled nerve group. The normal control group exhibited a dense, organized network of corneal nerves with extensive branching. In contrast, the pulled nerve group demonstrated reduced nerve density and disorganized nerve structures (Fig. 8A). Immunofluorescence analysis of *Krt16* in the corneal epithelium revealed significant differences between the normal control group and the pulled nerve group. In the normal control group, *Krt16* expression was minimal and confined to basal levels, reflecting normal epithelial homeostasis. However, in the pulled nerve group, *Krt16* expression was markedly upregulated, with strong localization in regions of epithelial detachment and structural disruption (Fig. 8B). Quantitative analysis revealed significant differences in corneal nerve density between the normal control group and the pulled nerve group. The pulled nerve group demonstrated a marked reduction in nerve density compared to the normal control group (Fig. 8C).

Krt16 Expression is Elevated in the Pulled Nerve Group

The pulled nerve group showed markedly increased *Krt16* expression compared to the normal control group (Fig. 8D).

Investigative Ophthalmology & Visual Science

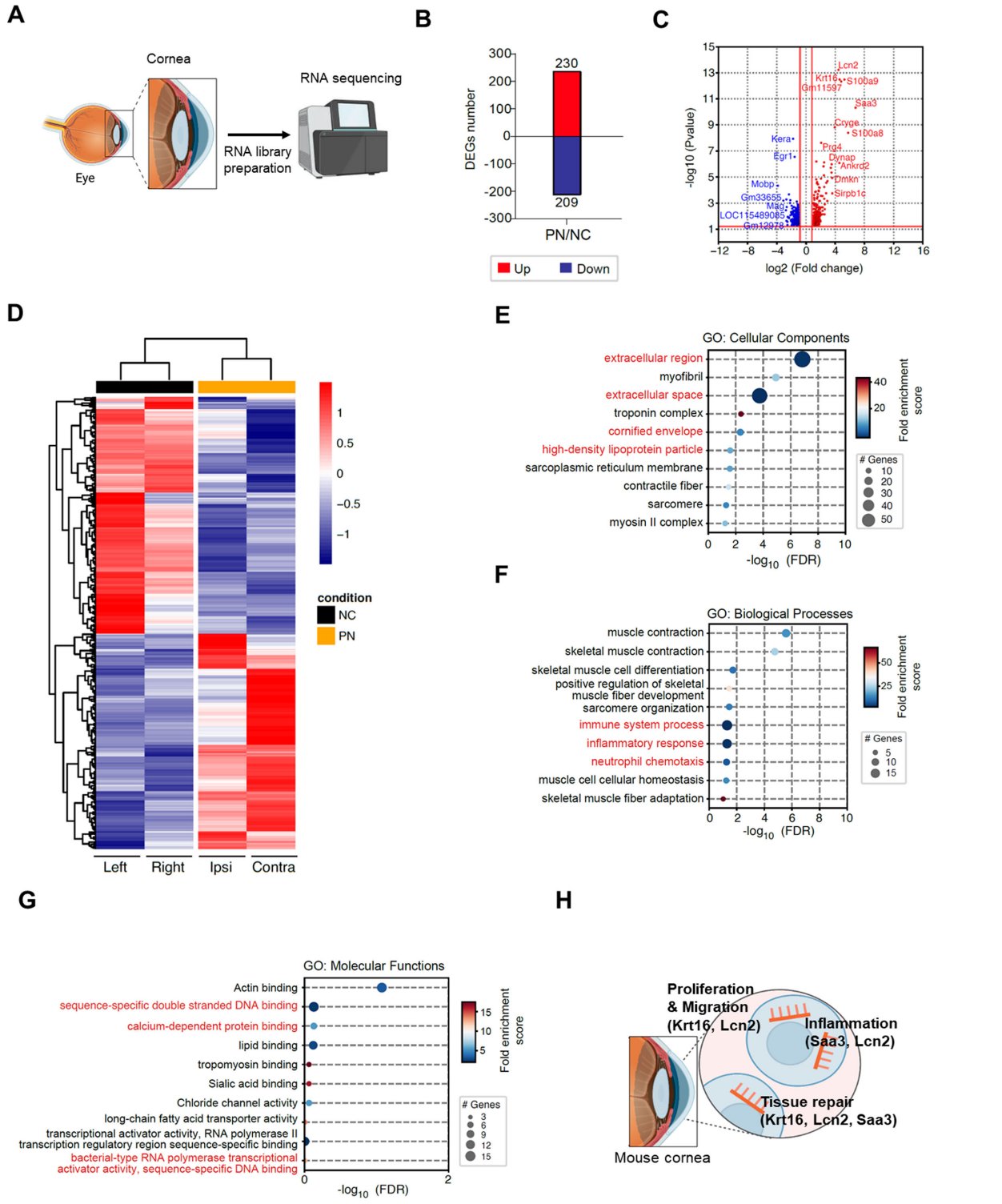

Figure 6. Gene expression and pathway analysis in neuropathic corneal pain model. (**A**) Schematic representation of RNA isolation from the cornea of normal control and pulled nerve models, followed by next-generation sequencing (NGS; $n = 6$ in each model). (**B**) Bar graph showing the number of significantly upregulated (*red*) and downregulated (*blue*) genes in the pulled nerve model compared to normal control, based on fold change and *P* value. (**C**) Volcano plot displaying differential gene expression analysis between normal control and pulled nerve corneal RNA samples. Significantly upregulated genes in pulled nerve are indicated by the *red dots*, and downregulated genes by the *blue dots*. The *dashed lines* mark the boundaries for genes with significantly altered expression (adjusted *P* value < 0.05 and log2 fold change). (**D**) Heat map representing hierarchical clustering of differentially expressed genes between normal control and pulled nerve corneas. The map shows normalized and variance-stabilized expression values. (**E**) Gene ontology (GO) Cellular Component analysis of differentially expressed genes, highlighting extracellular region, extracellular space, and cornified envelope. (**F**) GO Biological Process analysis, emphasizing immune system processes, inflammatory response, and neutrophil chemotaxis. (**G**) GO Molecular Function analysis, highlighting DNA binding and protein binding functions. (**H**) Hypothetical model illustrating the underlying mechanisms and key genes involved in the pulled nerve model, focusing on inflammation, proliferation, migration, and tissue repair processes. Key genes, such as *Krt16*, *Lcn2*, and *Saa3* are emphasized for their roles in these processes.

Investigative Ophthalmology & Visual Science

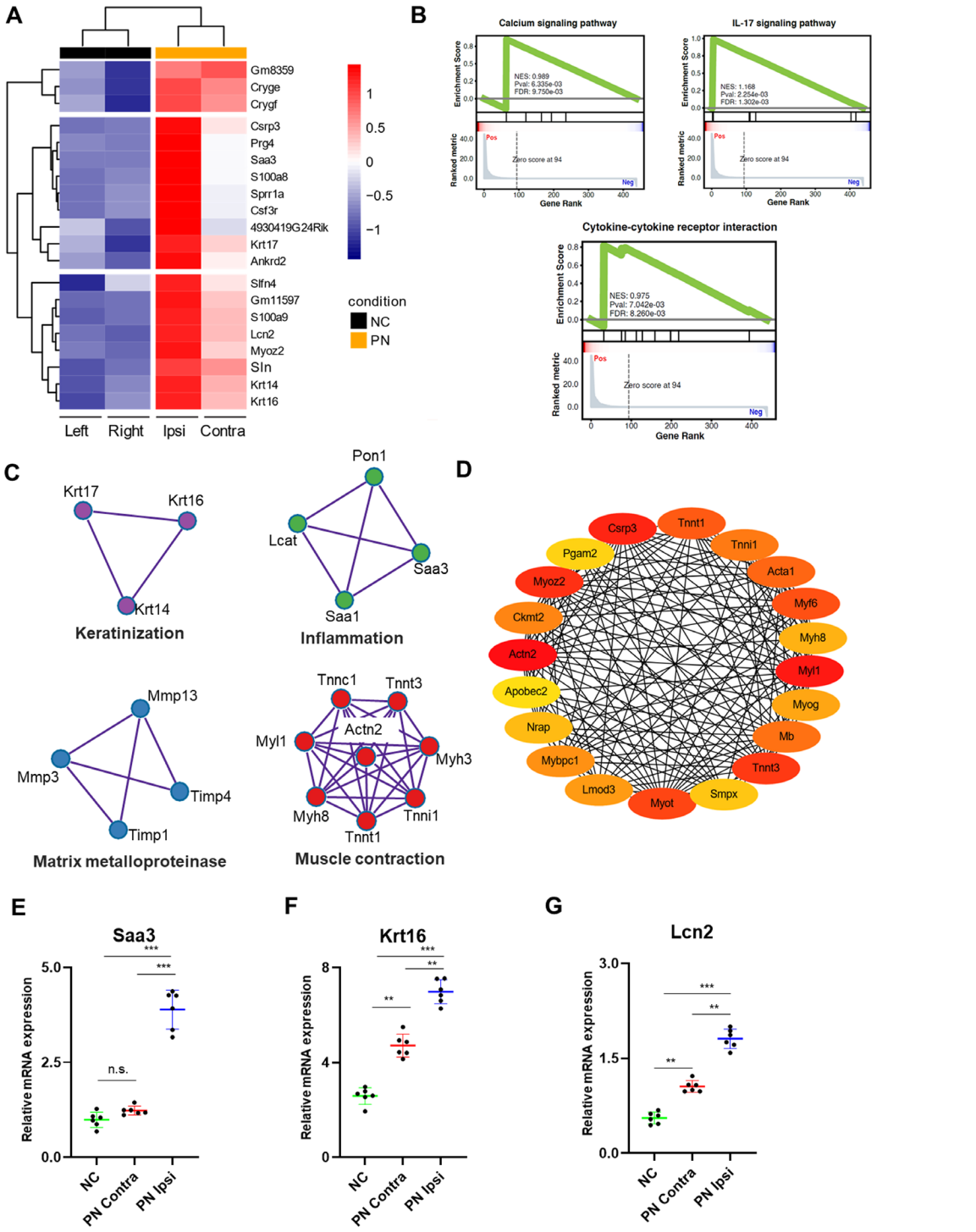

Figure 7. Analysis and validation of differential gene expression in neuropathic corneal pain model. (**A**) Gene expression data from RNA-seq were processed to normalize and identify the 20 most abundant transcript genes between the normal control models and the pulled nerve models. The magnitude of expression differences log2 fold change is indicated by different colors in the heat map from *red* (large increase in relative expression) to *blue* (large decrease in relative expression). (**B**) GSEA plot (KEGG pathways) of the top three significantly enriched terms in pulled nerve versus normal nerve positively correlated were the calcium signaling pathway, cytokine-cytokine receptor interaction pathway, and IL-17 signaling pathway. The *P* values and enrichment scores were calculated using the GSEA empirical phenotype-based permutation test, without adjustments for multiple comparisons. (**C**) Protein-protein interaction of four MCODE complexes identified in Metascape, colored by their identities. Their functional labels are generated based on the top-three functional enriched terms. (**D**) Representation of the top 20 hub genes, with high-ranking nodes highlighted in *red* and low-ranking nodes in *yellow*, determined by their ranking scores using the maximum clique centrality (MCC) method in the cytoHubba plugin of Cytoscape. These genes, identified as hub genes, demonstrate their network relationships. (**E**, **F**, **G**) Comparison of RNA-seq and qRT-PCR data. Mean values of RNAseq and qRT-PCR corresponding to *Saa3*, *Lcn2*, and *Krt16* genes analyzed between corneas of normal control and pulled nerve models, converted to log2 fold change and used to verify the two methods. Bar charts demonstrate statistical significance of normal control, pulled nerve contralateral, and pulled nerve ipsilateral. Error bars represent standard deviation between biological replicates ($n = 6$ in each model), and significance was calculated with 1-way ANOVA with Tukey's multiple comparisons test, where: $^{*}P < 0.05$, $^{**}P < 0.01$, and $^{***}P < 0.001$, ns = not significant.

Investigative Ophthalmology & Visual Science

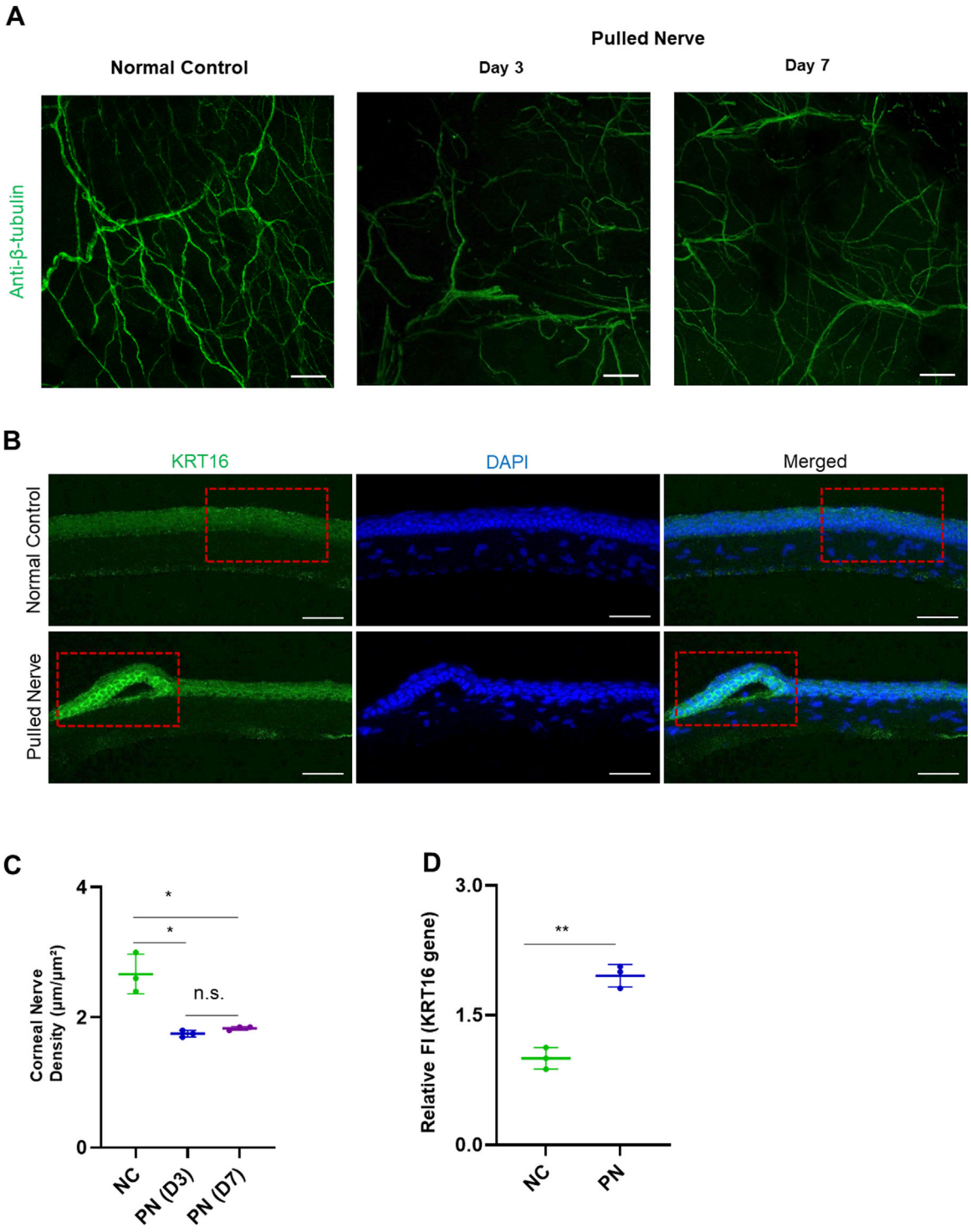

Figure 8. Corneal nerve morphology and *Krt16* gene expression in corneal epithelium in neuropathic corneal pain. (**A**) Representative confocal images of corneal nerves stained with anti-β-tubulin, showing structural changes in the normal control group and the pulled nerve group. The images highlight variations in nerve density, branching, and organization. Scale bars represent 50 µm. (**B**) Immunofluorescence images of corneal epithelial sections stained for *Krt16* (*green*) and nuclei (DAPI, *blue*) in the normal control group and the pulled nerve group. The normal control group shows minimal *Krt16* expression, indicative of normal epithelial homeostasis. In contrast, the pulled nerve group exhibits heightened *Krt16* expression, particularly localized in regions of epithelial detachment and disruption (highlighted by *red dashed boxes*). Scale bars represent 50 µm. (**C**) Comparison of corneal nerve density between the normal control group and the pulled nerve group. This reduction highlights structural changes in corneal nerves associated with the pulled nerve model of neuropathic corneal pain. Data points represent the mean values (±SD) for 3 mice each at D3 and D7 post-surgery. Statistical significance is indicated by $^{*}P < 0.05$, $^{**}P < 0.01$, $^{***}P < 0.001$, $^{****}P < 0.0001$. (**D**) Quantitative analysis of *Krt16* expression in the corneal epithelium between the normal control and the pulled nerve groups. The pulled nerve group exhibited significantly higher *Krt16* expression compared to the normal control. This increase indicates heightened epithelial stress in the pulled nerve model, consistent with neuropathic corneal pain. Data points represent the mean values (±SD) for 3 mice at D15 post-surgery. Statistical significance is indicated by $^{*}P < 0.05$, $^{**}P < 0.01$, $^{***}P < 0.001$, $^{****}P < 0.0001$.

Investigative Ophthalmology & Visual Science

Discussion

Originating primarily from neuropathy, the NP presents across various anatomic regions, exhibiting diverse pain levels due to malfunctioning nerves harboring different types of sensory receptors, including nociceptors, mechanoreceptors, and chemoceptors.[42,43] Our proposed model delineates key aspects of NCP, faithfully capturing nociception, ocular irritation, and its transition into the chronic stage. Neuronal hyperexcitability, a hallmark of NP, is typically evaluated by delineating affected areas to identify stimuli eliciting allodynia or hyperalgesia (Supplementary Tables S3A, S3B). Consistent with this approach, we established the relationship between applied noxious stimuli and perceived pain using chemical challenge (i.e. NaCl solutions), quantifying the characteristic status of NCP through estimating curve fit variables. Stevens' Power Law is a psychophysical theory that describes the relationship between the magnitude of a physical stimulus (chemical test) and the perceived intensity (perception of pain) of that stimulus. It was proposed by American psychologist Stanley Smith Stevens in 1957 as an extension and refinement of Fechner's Law.[44] The strength of our NCP model lies in its ability to represent key features of human NCP, including the characterization of power law dynamics in the pain-perception relationship, providing new insights into pain measurement in an animal model. Although the model successfully mimics certain aspects of patient experiences, we recognize that it does not fully replicate all characteristics of human neuropathy. This approach contributes to a more robust framework for assessing pain status in controlled experimental settings, aiding the development of targeted therapies.

Existing animal models of neuropathic pain like chronic constriction injury (CCI) to the sciatic nerve, partial sciatic nerve ligation (pSNL), spinal nerve ligation (SNL), spared nerve injury (SNI), brachial plexus avulsion (BPA), sciatic nerve transaction (SNT), and sciatic nerve trisection vary based on the location and type of nerve injury.[45,46] Over the past decades, numerous models have been developed to study nerve damage and the resulting NP. Given the diversity of human peripheral neuropathies, no single animal model can fully replicate all aspects of these conditions. However, each model has made valuable contributions to advancing our understanding of neuropathic pain mechanisms.[45]

Supplemental Table S4 summarizes features of existing corneal experimental animal models and lists advantages and disadvantages of each approach. Previously, Anderson et al.[21] used the chemical burn, which would cause the destruction of terminal nerve endings, thus undermining the naturalistic setting of NCP. Meanwhile, Kennedy et al.[22] examined the effects of UV light, which could alter the mechanisms underlying NCP by dismantling the structural composites, such as corneal epithelial, keratocyte, and endothelial cells. In this regard, we showed in the current study that the detachment of the epithelial layer, not directly caused by physical damage, may serve as an indicator of underlying neuropathic mechanisms. This observation aligns with previous studies suggesting that neuropathic alterations in corneal innervation can manifest as epithelial abnormalities,[47,48] further demonstrating the consistency of the proposed NCP model. Hence, our pulled nerve model realistically highlights the complex interplay between corneal nerve dysfunction and structural changes in neuropathic conditions.

As for surgical modifications, Fakih et al.[49] conducted excisions of the extraorbital lacrimal gland and Harderian gland, an acute stage NP study cannot be conducted due to the extended recovery time. Inomata et al.,[50] on the other hand, used the intrastromal suture method, its utility is limited to related diseases, such as lymphangiogenesis-induced NCP. Last, Seyed-Razavi et al.[23,24] and Wu et al.[25] described the ciliary nerve-ligation method, currently the most widely used approach for creating NCP models. This technique involves the ligation of ciliary nerves to prevent epithelial defects and corneal nerve avulsion. However, it requires meticulous dissection and precise tissue manipulation, necessitating complex surgical techniques. In contrast, our NCP model offers potential benefits in terms of procedural simplicity and reduced invasiveness, which may contribute to improved survival outcomes and shorter surgical durations, based on comparative assessments of nerve manipulation techniques (Supplementary Table S5), making it valuable for investigating various aspects of NCP and related mechanisms.

In all three surgical models (i.e. sham control, pulled nerve, and full transection), significant reductions in the mechanical pain threshold (determined by von Frey) were observed post-surgery, persisting until the end point of the study (i.e. D14), likely due to sustained activation of mechanonociceptors.[51,52] As shown in Figure 2C, the von Frey thresholds in both pulled nerve and full transection groups gradually improved over time, whereas those in the sham control group remained relatively stable from D1 to D14. This trend suggests a potential dose-response relationship between nerve injury severity and regeneration processes, which aligns with previous findings that emphasize the impact of injury severity on nerve regeneration outcomes.[53] Additionally, other experimental evidence indicates that the extent of nerve damage correlates with Schwann cell proliferation and axonal sprouting during regeneration.[54] Interestingly, despite consistently greater pain susceptibility than the normal control group, all three surgical groups, including sham control, exhibited converging von Frey pain thresholds toward a single recovery value by D14. Sham surgeries in many nerve injury models often result in damage to deeper tissues. Additionally, both mild incision models and more invasive postsurgical models in rodents can lead to varying degrees of behavioral hypersensitivity, from transient to chronic pain, as well as increased nociceptor excitability.[55–58] This convergence, which implies a shared sensitization mechanism among the groups, suggests the progression to the chronic stage of NCP, irrespective of nerve damage level. Therefore, understanding the relationship between nerve injury severity and regeneration capacity is vital to develop effective therapeutic interventions aimed at promoting nerve repair and functional recovery.

In contrast to the response to chemical stimuli, some mice in the normal control group exhibited highly desensitized von Frey responses at D1 and subsequently at D7 and D14. One factor likely to explain such variability is the acute stress response arising from the inhibition of the pain system.[59–64] Additionally, the von Frey test outcomes of the sham control group were notably distinguishable from those of the normal control group, indicating a meaningful impact of the sham surgery on corneal sensory function. This disparity between the stimulation types may arise from the possible fact that surgery-induced Wallerian degeneration of nerves innervat-

Investigative Ophthalmology & Visual Science

ing the surrounding tissue differently affects the corneal nociceptive receptors.[65]

In our study, chemical stimuli-induced pain was used to modulate stimulus intensity. Specifically, Stevens' Law concept, which suggests a power dependence between stimulus intensity and perception strength, was used in chemical test for post-injury pain, potentially including allodynia and hyperalgesia.[26,66] For each animal group, the power exponents (Alpha values) were obtained with high R^2 values (>0.94), effectively differentiating NCP models. These Alpha differences between NCP models suggest potential application of pain-perception measurements for unbiased monitoring of individual differences and NCP progression. Additionally, the strong correlations observed between the behavioral parameter based on the chemical stimulus (i.e. Alpha) and TG SGCs ($|r| > 0.92$), and neuron ($|r| > 0.86$) densities imply the diagnostic capability of Alpha for assessing neural damage at the cellular level.

Despite the extensive research on NCP involving ciliary nerves, there remains a notable gap in understanding how ciliary nerve damage impacts corneal tissue.[34] Given the role of changes in neural circuitry and plasticity within the cornea and associated nerve pathways in abnormal pain signaling, we posit that NCP-related alterations in corneal tissue structural integrity, such as epithelial or stromal layer deterioration, may heighten sensitivity and pain perception. Histopathological analysis of the cornea revealed widespread structural changes in all three experimental groups, supporting the plausibility of this hypothesis. Consistent with previous findings, epithelial layer exfoliation likely precedes subsequent pathogenic and inflammatory alterations in the cornea.[67] The *Krt16* gene plays a role in the migration of keratinocytes[68,69] and the proliferation of epithelial cells.[68,70] The outcomes of our study align with the results observed by Liu et al.,[70] as detachment of the corneal epithelium was seen in our pulled nerve model of NCP (see Fig. 4A). The inability to properly regulate the proliferation and differentiation of epithelial cells can result in the loss of epithelial integrity and subsequent detachment.[71,72] Upon histological examination, distinct surgery-dependent changes in the corneal tissue structure were evident across all animal groups, including sham control. Particularly noteworthy were the significant structural changes, such as decreased epithelial thickness, observed in the sham control group compared to the normal control group. These changes, in conjunction with significant behavioral alterations (e.g. von Frey threshold), underscore the association between structural corneal damage and the development and progression of NCP. Given that in sham control models, the NCP-causing injury occurs in tissues unrelated to the corneal nerves, the observed structural changes in the cornea alone could serve as initiating factors for neuropathic dysfunction. The clinical significance underscores the importance of this phenomenon, as it closely parallels the human NCP framework, where direct nervous system damage is typically absent. This prompts further exploration of peripheral tissue damage as a potential cause of NP, warranting future investigations. The observed reductions in corneal nerve density and structural organization are consistent with previous reports of corneal nerve injury[24] contributing to the pathophysiology of NCP.

An injury affecting the corneal nociceptors disrupts afferent input, leading to abnormal signal processing within the neural circuits of the TG complex and consequent central sensitization.[51,52] Within the TG, neurons and SGCs are organized into distinct bands or clusters. SGCs envelop the cell bodies of TG neurons, providing metabolic support, physical protection, and maintaining neuronal homeostasis, whereas also modulating neurotransmitter levels and releases.[73–75] Moreover, SGCs respond to stress or injury signals from neurons, particularly in peripheral injuries that cause inflammation and pain.[74,76] Our findings demonstrate variations in SGCs counts across the animal models (normal control, sham control, full transection, and pulled nerve), indicating altered SGCs populations in the context of NCP severity. In this regard, the observed linear relationship between Alpha values and SGCs counts (as shown in Fig. 5H) offers a novel, nonterminal means for quantifying histological measures without model sacrifice. We hypothesize that dysregulated interactions involving SGCs contribute to corneal pain development and chronicity, potentially offering new therapeutic avenues. Future investigations will incorporate Western blot analysis (GFAP expression) and other molecular approaches to confirm and extend our quantitative assessments for validation of SGC numbers.

Moreover, RNA-seq and differential expression analysis revealed that genes involved in inflammation, immune response, and extracellular matrix organization were prominently affected. This indicates a multifaceted biological response to neuropathic injury, encompassing inflammation, tissue remodeling, and immune activation. We chose the pulled nerve model for this study due to its ability to mimic a more gradual and moderate injury, which closely resembles certain clinical scenarios of corneal neuropathy. Key genes, such as *Saa3* (responsible for inflammatory and wound healing responses in cornea),[77,78] *Lcn2* (regulating cell adhesion/migration, autophagy, inflammation, post-translational modifications, and cell immune functions),[79,80] and *Krt16* (cell adhesion and immigration, epithelial cell proliferation)[68,81] are highlighted for their roles in these processes, indicating their potential as therapeutic targets. The substantial increase underscores the *Krt16* gene's significant upregulation in response to the pulled nerve model, suggesting a crucial role in the biological processes involved. Comparison of RNA-seq and qRT-PCR data shows strong consistency between the two methods, with significant differences in gene expression between the normal control model and the pulled nerve model. The significant upregulation of *Krt16* in the pulled nerve model suggests a crucial role for this gene in the pathophysiology of NCP. *Krt16* is involved in maintaining epithelial barrier integrity, responding to stress and injury, and modulating inflammatory responses. The observed upregulation aligns with histological findings showing LCN elongation, thickening, and corneal tissue alterations in the pulled nerve models. The elevated *Krt16* expression observed in the pulled nerve model of neuropathic corneal pain highlights its role as a marker of epithelial stress and injury. We also hypothesized that the corneal epithelium might play a role in the pulled nerve model of NCP through the contribution of *Krt16* gene.

Conclusions

The development of a robust murine model is pivotal for translational studies, facilitating the transition from preclinical investigations to clinical interventions. Our enhanced ability to quantify NCP features, particularly through quantitative pain measures such as the NaCl challenge, not only opens new avenues for research but also enriches the methodological repertoire for evaluating treatment efficacy.

Investigative Ophthalmology & Visual Science

The *Krt16* gene emerges as a promising target for NCP. Thus, our study significantly advances the understanding of NCP pathogenesis and offers new avenues for developing targeted treatments.

Acknowledgments

Supported by the AI-based GIST Research Scientist Project grant funded by the GIST in 2025, the National Research Foundation of Korea (NRF) grant funded by the Korea government (MSIT; No. RS-2023-00264409 and No. RS-2023-00302281), and the Brain Pool program funded by the Ministry of Science and ICT through the NRF of Korea (RS-2023-00304323). We are very thankful to Doyun Kim, Pf. Seog bae Oh (SNU), and Geehun Jeong (Neurogrin) for helpful discussion on the manuscript. We extend our gratitude to Haewon Chung for the English language corrections and to Daeun Roh for a schematic preparation. Additionally, we would like to thank Tien Nhat Nguyen, Christine H. Hwang, and Akm Ashiquzzaman for their assistance with the behavioral tests.

Author Contributions: M.A.K. and E.C. conceptualized, designed, and directed the research. M.A.K. drafted the manuscript. Y.R.K. updated manuscript and guided the research. M.A.K. conducted experiments and analyzed data. G.F. drew the schematics, helped in figure panel design, GraphPad analysis, and revised the manuscript. A.E. performed RNA sequencing and qRT-PCR analysis. S.S.K., H.S.K., and K.C.Y. gave feedbacks on the manuscript and helped experimental design.

Data Availability Statements: The authors confirm that the primary data supporting the conclusions of this study are included within the article and its Supplementary information files. For further inquiries and material requests, please contact Euiheon Chung (EC). This study involves data deposition in external repositories (BioProject ID: PRJNA1158961).

Disclosure: **M.A. Khan**, None; **G. Fatima**, None; **A. Emmanuel**, None; **S.S. Kim**, None; **H.S. Kwon**, None; **K.C. Yoon**, None; **Y.R. Kim**, None; **E. Chung**, None

References

1. Dworkin RH, O'Connor AB, Kent J, et al. Interventional management of neuropathic pain: NeuPSIG recommendations. *Pain*. 2013;154(11):2249–2261.
2. Dieckmann G, Goyal S, Hamrah P. Neuropathic corneal pain: approaches for management. *Ophthalmology*. 2017;124(11):S34–S47.
3. Greenspan JD. Quantitative assessment of neuropathic pain. *Curr Pain Headache Rep*. 2001;5(2):107–113.
4. Rosenthal P, Borsook D. The corneal pain system. Part I: the missing piece of the dry eye puzzle. *Ocul Surf*. 2012;10(1):2–14.
5. Rosenthal P, Borsook D. Ocular neuropathic pain. *Br J Ophthalmol*. 2016;100(1):128–134.
6. Rosenthal P, Borsook D, Moulton EA. Oculofacial pain: corneal nerve damage leading to pain beyond the eye. *Invest Ophthalmol Vis Sci*. 2016;57(13):5285–5287.
7. Aggarwal S, Kheirkhah A, Cavalcanti BM, et al. Autologous serum tears for treatment of photoallodynia in patients with corneal neuropathy: efficacy and evaluation with in vivo confocal microscopy. *Ocul Surf*. 2015;13(3):250–262.
8. Hamrah P, Qazi Y, Shahatit B, et al. Corneal nerve and epithelial cell alterations in corneal allodynia: an in vivo confocal microscopy case series. *Ocul Surf*. 2017;15(1):139–151.
9. Watson SL, Le DT-M. Corneal neuropathic pain: a review to inform clinical practice. *Eye (Lond)*. 2024;38:2350–2358.
10. Belmonte C. Eye dryness sensations after refractive surgery: impaired tear secretion or "phantom" cornea? *J Refract Surg*. 2007;23(6):598–602.
11. Rosenthal P, Baran I, Jacobs DS. Corneal pain without stain: is it real? *Ocul Surf*. 2009;7(1):28–40.
12. Ebrahimiadib N, Yousefshahi F, Abdi P, Ghahari M, Modjtahedi BS. Ocular neuropathic pain: an overview focusing on ocular surface pains. *Clin Ophthalmol (Auckland, NZ)*. 2020;14:2843.
13. Belmonte C, Giraldez F. Responses of cat corneal sensory receptors to mechanical and thermal stimulation. *J Physiol*. 1981;321(1):355–368.
14. Galor A, Levitt RC, Felix ER, Sarantopoulos CD. Understanding the true burden of dry eye disease. *Expert Rev Ophthalmol*. 2015;10(5):403–405.
15. Theophanous C, Jacobs DS, Hamrah P. Corneal neuralgia after LASIK. *Optom Vis Sci*. 2015;92(9):e233–e240.
16. Galor A, Levitt R, Felix E, Martin E, Sarantopoulos C. Neuropathic ocular pain: an important yet underevaluated feature of dry eye. *Eye*. 2015;29(3):301–312.
17. Guerrero-Moreno A, Baudouin C, Melik Parsadaniantz S, Réaux-Le Goazigo A. Morphological and functional changes of corneal nerves and their contribution to peripheral and central sensory abnormalities. *Front Cell Neurosci*. 2020;14:610342.
18. Yamaguchi T, Turhan A, Harris DL, et al. Bilateral nerve alterations in a unilateral experimental neurotrophic keratopathy model: a lateral conjunctival approach for trigeminal axotomy. *PLoS One*. 2013;8(8):e70908.
19. Vereertbrugghen A, Galletti JG. Corneal nerves and their role in dry eye pathophysiology. *Exp Eye Res*. 2022;222:109191.
20. McKay TB, Seyed-Razavi Y, Ghezzi CE, et al. Corneal pain and experimental model development. *Prog Retin Eye Res*. 2019;71:88–113.
21. Anderson C, Zhou Q, Wang S. An alkali-burn injury model of corneal neovascularization in the mouse. *J Vis Exp*. 2014;(86):e51159.
22. Kennedy M, Kim KH, Harten B, et al. Ultraviolet irradiation induces the production of multiple cytokines by human corneal cells. *Invest Ophthalmol Vis Sci*. 1997;38(12):2483–2491.
23. Seyed-Razavi Y, Lopez MJ, Yamaguchi T, Hamrah P. A novel experimental model for corneal neuropathic pain: the ciliary nerve ligation approach. *Invest Ophthalmol Vis Sci*. 2017;58(8):3951.
24. Seyed-Razavi Y, Kenyon BM, Qiu F, Harris DL, Hamrah P. A novel animal model of neuropathic corneal pain–the ciliary nerve constriction model. *Front Neurosci*. 2023;17:1265708.
25. Wu J, Yuan T, Fu D, et al. An experimental model for primary neuropathic corneal pain induced by long ciliary nerve ligation in rats. *Pain*. 2024;165(6):1391–1403.
26. Bolton ML, Ed. Modeling human perception Could Stevens' Power Law be an emergent feature? *2008 IEEE International Conference on Systems, Man and Cybernetics*. 2008: IEEE.
27. Lessard JC, Piña-Paz S, Rotty JD, et al. Keratin 16 regulates innate immunity in response to epidermal barrier breach. *Proc Natl Acad Sci*. 2013;110(48):19537–19542.
28. Lupasco T, He Z, Cassagne M, et al. Corneal epithelium in keratoconus underexpresses active NRF2 and a subset of oxidative stress-related genes. *PLoS One*. 2022;17(10):e0273807.
29. McGuire J, Osber M, Lightfoot L. Two keratins MW 50,000 and 56,000 are synthesized by psoriatic epidermis. *Br J Dermatol*. 1984;111(s27):27–37.
30. Schermer A, Jester JV, Hardy C, Milano D, Sun T-T. Transient synthesis of K6 and K16 keratins in regenerating rabbit corneal epithelium: keratin markers for an alterna-

tive pathway of keratinocyte differentiation. *Differentiation*. 1989;42(2):103–110.

31. Tajerian M, Hung V, Khan H, et al. Identification of KRT16 as a target of an autoantibody response in complex regional pain syndrome. *Exp Neurol*. 2017;287:14–20.
32. Paris F, Hurtado C, Azon A, Aguado L, Vizmanos JL. A new KRT 16 mutation associated with a phenotype of pachyonychia congenita. *Exp Dermatol*. 2013;22(12):838–839.
33. Ren K. An improved method for assessing mechanical allodynia in the rat. *Physiol Behav*. 1999;67(5):711–716.
34. Joubert F, Acosta MdC, Gallar J, et al. Effects of corneal injury on ciliary nerve fibre activity and corneal nociception in mice: a behavioural and electrophysiological study. *Eur J Pain*. 2019;23(3):589–602.
35. Deuis JR, Dvorakova LS, Vetter I. Methods used to evaluate pain behaviors in rodents. *Front Molec Neurosci*. 2017;10:284.
36. Farazifard R, Safarpour F, Sheibani V, Javan M. Eye-wiping test: a sensitive animal model for acute trigeminal pain studies. *Brain Res Brain Res Protoc*. 2005;16(1–3):44–49.
37. Lemp A. Report of the National Eye Institute/Industry workshop on clinical trials in dry eyes. *CLAO J*. 1995;21(4):221–232.
38. Sherman BT, Hao M, Qiu J, et al. DAVID: a web server for functional enrichment analysis and functional annotation of gene lists (2021 update). *Nucleic Acids Res*. 2022;50(W1):W216–W221.
39. Shannon P, Markiel A, Ozier O, et al. Cytoscape: a software environment for integrated models of biomolecular interaction networks. *Genome Res*. 2003;13(11):2498–2504.
40. Zhou Y, Zhou B, Pache L, et al. Metascape provides a biologist-oriented resource for the analysis of systems-level datasets. *Nat Commun*. 2019;10(1):1523.
41. Roch M, Messlinger K, Kulchitsky V, Tichonovich O, Azev O, Koulchitsky S. Ongoing activity in trigeminal wide-dynamic range neurons is driven from the periphery. *Neuroscience*. 2007;150(3):681–691.
42. Costigan M, Scholz J, Woolf CJ. Neuropathic pain: a maladaptive response of the nervous system to damage. *Annu Rev Neurosci*. 2009;32:1–32.
43. Finnerup NB, Kuner R, Jensen TS. Neuropathic pain: from mechanisms to treatment. *Physiol Rev*. 2021;101:259–301.
44. Stevens SS. On the psychophysical law. *Psychol Rev*. 1957;64(3):153–181.
45. Challa SR. Surgical animal models of neuropathic pain: Pros and Cons. *Int J Neurosci*. 2015;125(3):170–174.
46. Dowdall T, Robinson I, Meert TF. Comparison of five different rat models of peripheral nerve injury. *Pharmacol Biochem Behav*. 2005;80(1):93–108.
47. Mastropasqua L, Massaro-Giordano G, Nubile M, Sacchetti M. Understanding the pathogenesis of neurotrophic keratitis: the role of corneal nerves. *J Cell Physiol*. 2017;232(4):717–724.
48. Al-Aqaba MA, Dhillon VK, Mohammed I, Said DG, Dua HS. Corneal nerves in health and disease. *Prog Retin Eye Res*. 2019;73:100762.
49. Fakih D, Zhao Z, Nicolle P, et al. Chronic dry eye induced corneal hypersensitivity, neuroinflammatory responses, and synaptic plasticity in the mouse trigeminal brainstem. *J Neuroinflammation*. 2019;16(1): 268.
50. Inomata T, Mashaghi A, Di Zazzo A, Dana R. Ocular surgical models for immune and angiogenic responses. *J Biol Methods*. 2015;2(3):e27.
51. Belmonte C, Acosta MC, Merayo-Lloves J, Gallar J. What causes eye pain? *Curr Ophthalmol Rep*. 2015;3(2):111–121.
52. Launay P-S, Reboussin E, Liang H, et al. Ocular inflammation induces trigeminal pain, peripheral and central neuroinflammatory mechanisms. *Neurobiol Dis*. 2016;88:16–28.
53. Wang D, Fawcett J. The perineuronal net and the control of CNS plasticity. *Cell Tissue Res*. 2012;349:147–160.
54. Arthur-Farraj PJ, Latouche M, Wilton DK, et al. c-Jun reprograms Schwann cells of injured nerves to generate a repair cell essential for regeneration. *Neuron*. 2012;75(4):633–647.
55. Odem MA, Lacagnina MJ, Katzen SL, et al. Sham surgeries for central and peripheral neural injuries persistently enhance pain-avoidance behavior as revealed by an operant conflict test. *Pain*. 2019;160(11):2440–2455.
56. Banik RK, Brennan TJ. Sensitization of primary afferents to mechanical and heat stimuli after incision in a novel in vitro mouse glabrous skin-nerve preparation☆. *Pain*. 2008;138(2):380–391.
57. Brennan TJ, Vandermeulen EP, Gebhart G. Characterization of a rat model of incisional pain. *Pain*. 1996;64(3):493–502.
58. Cao J, Wang P-K, Tiwari V, et al. Short-term pre-and post-operative stress prolongs incision-induced pain hypersensitivity without changing basal pain perception. *Mol Pain*. 2015;11:73.
59. Vachon-Presseau E, Martel M-O, Roy M, et al. Acute stress contributes to individual differences in pain and pain-related brain activity in healthy and chronic pain patients. *J Neurosci*. 2013;33(16):6826–6833.
60. Madden IV J, Akil H, Patrick RL, Barchas JD. Stress-induced parallel changes in central opioid levels and pain responsiveness in the rat. *Nature*. 1977;265(5592):358–360.
61. Willer JC, Dehen H, Cambier J. Stress-induced analgesia in humans: endogenous opioids and naloxone-reversible depression of pain reflexes. *Science*. 1981;212(4495):689–691.
62. Akil H, Young EA, Walker JM, Watson SJ. The many possible roles of opioids and related peptides in stress-induced analgesia. *Ann N Y Acad Sci*. 1986;467:140–153.
63. Hohmann AG, Suplita RL, Bolton NM, et al. An endocannabinoid mechanism for stress-induced analgesia. *Nature*. 2005;435(7045):1108–1112.
64. Butler RK, Finn DP. Stress-induced analgesia. *Prog Neurobiol*. 2009;88(3):184–202.
65. Dubový P. Wallerian degeneration and peripheral nerve conditions for both axonal regeneration and neuropathic pain induction. *Ann Anat*. 2011;193(4):267–275.
66. Lolignier S, Eijkelkamp N, Wood JN. Mechanical allodynia. *Pflügers Arch*. 2015;467(1):133–139.
67. Shimizu S, Sato S, Taniguchi H, et al. Observation of chronic graft-versus-host disease mouse model cornea with in vivo confocal microscopy. *Diagnostics*. 2021;11(8):1515.
68. Jia J, Han Y, Jin L, et al. miR-204-3p downregulates KRT16 and promotes corneal repair in tree shrew fungal keratitis model. *Am J Transl Res*. 2022;14(10):7336.
69. Jia J, Wang W, Kuang D, et al. mRNA profiling reveals response regulators of decreased fungal keratitis symptoms in a tree shrew model. *Gene*. 2020;737:144450.
70. Liu L, Li Y-P, Huang S-Q, Lin J-X, Zhang W-X. Mechanism of keratinocyte growth factor-2 accelerating corneal epithelial wound healing on rabbit alkali burned cornea [in Chinese]. *Zhonghua Yan Ke Za Zhi*. 2005;41(4):364–368.
71. Ruan Y, Jiang S, Musayeva A, Pfeiffer N, Gericke A. Corneal epithelial stem cells–physiology, pathophysiology and therapeutic options. *Cells*. 2021;10(9):2302.
72. Thoft RA, Friend J. The X, Y, Z hypothesis of corneal epithelial maintenance. *Invest Ophthalmol Vis Sci*. 1983;24(10):1442–1443.
73. Hanani M. Satellite glial cells in sensory ganglia: from form to function. *Brain Res Rev*. 2005;48(3):457–476.

Investigative Ophthalmology & Visual Science

74. Durham PL, Garrett F. Emerging importance of neuron-satellite glia interactions within trigeminal ganglia in craniofacial pain. *Open Pain J*. 2010;3:3–13.
75. Takeda M, Kitagawa J, Takahashi M, Matsumoto S. Activation of interleukin-1β receptor suppresses the voltage-gated potassium currents in the small-diameter trigeminal ganglion neurons following peripheral inflammation. *Pain*. 2008;139(3):594–602.
76. Huang T-Y, Belzer V, Hanani M. Gap junctions in dorsal root ganglia: possible contribution to visceral pain. *Eur J Pain*. 2010;14(1):49.e1–e11.
77. Chakravarti S, Wu F, Vij N, Roberts L, Joyce S. Microarray studies reveal macrophage-like function of stromal keratocytes in the cornea. *Invest Ophthalmol Vis Sci*. 2004;45(10):3475–3484.
78. Jia C, Zhu W, Ren S, Xi H, Li S, Wang Y. Comparison of genome-wide gene expression in suture-and alkali burn-induced murine corneal neovascularization. *Mol Vis*. 2011;17:2386.
79. Ghosh S, Stepicheva N, Yazdankhah M, et al. The role of lipocalin-2 in age-related macular degeneration (AMD). *Cell Mol Life Sci*. 2020;77:835–851.
80. Me R. LCN-2 enhances host defense against Pseudomonas aeruginosa infection in C57BL/6 mouse corneas. *Invest Ophthalmol Vis Sci*. 2023;64(8):1717.
81. Zhang W, Lan X, Zhu J, et al. Healing ability of central corneal epithelium in rabbit ocular surface injury models. *Transl Vis Sci Technol*. 2022;11(6):28.

Investigative Ophthalmology & Visual Science